DOKUZ EYLÜL UNIVERSITY

GRADUATE SCHOOL OF NATURAL AND APPLIED SCIENCES

DESIGN OF SYNTHESIS OF NEW GENERATION RARE EARTH DOPED $K_2Ln_2Ti_3O_{10}$ SEMICONDUCTING FILMS AND THEIR INDUSTRIAL APPLICATIONS

by

Özlem CANPOLAT

August, 2015

İZMİR

DESIGN OF SYNTHESIS OF NEW GENERATION RARE EARTH DOPED $K_2Ln_2Ti_3O_{10}$ SEMICONDUCTING FILMS AND THEIR INDUSTRIAL APPLICATIONS

A Thesis Submitted to the
Graduate School of Natural and Applied Sciences of Dokuz Eylül University
In Partial Fulfillment of the Requirements for the Degree of Master of Science in Metallurgical and Material Engineering

by
Özlem CANPOLAT

August, 2015
İZMİR

M.Sc THESIS EXAMINATION RESULT FORM

We have read the thesis entitled **"DESIGN OF SYNTHESIS OF NEW GENERATION RARE EARTH DOPED $K_2Ln_2Ti_3O_{10}$ SEMICONDUCTING FILMS AND THEIR INDUSTRIAL APPLICATIONS"** completed by **ÖZLEM CANPOLAT** under supervision of **PROF. DR. ERDAL ÇELİK** and we certify that in our opinion it is fully adequate, in scope and in quality, as a thesis for the degree of Master of Science.

Prof. Dr. Erdal ÇELİK

Supervisor

Prof. Dr. Mustafa TOPARLI

(Jury Member)

Prof. Dr. Ayşegül AKA

(Jury Member)

Prof. Dr. Ayşe OKUR

Director

Graduate School of Natural and Applied Sciences

ACKNOWLEDGEMENT

Firstly, I would like to thank Prof. Dr. Erdal ÇELİK for his supervision, guidance and support in this work.

I would also like to thank my committee members: Prof. Dr. Ayşegül PALA and Prof. Dr. Mustafa TOPARLI.

I am thankful to Assist. Prof. Dr. Mustafa EROL for his advices and comments.

I am grateful to Prof. Dr. Monika Willert-Poroda and her team for providing everything that made research possible during my Erasmus stay in Bayreuth University, Germany.

I wish to extend special thanks to Electronic Materials Production and Application Center (EMUM) and their very helpful personnels, especially my project mates Fatma BAKAL and Güneş KURŞUN.

I gratefully acknowledge the financial assistance provided by The Scientific and Technological Research Council of Turkey (TUBITAK), under project number 112Y162.

Finally, I would like to express my gratitude to my all family for their support and persistence.

Özlem CANPOLAT

DESIGN OF SYNTHESIS OF NEW GENERATION RARE EARTH DOPED $K_2Ln_2Ti_3O_{10}$ SEMICONDUCTING FILMS AND THEIR INDUSTRIAL APPLICATIONS

ABSTRACT

In this study synthesis and characterization of K2*Ln*2Ti3O10 (Ln; La, Nd, Gd, Sm, Dy) thin films were investigated for photocatalyic applications. Newly developed layered perovskite structures are produced by sol-gel method. With this aim, transparent solutions were prepared from K, Ti, La, Nd , Gd, Sm and Dy based precursors, propionic acid and glacial acetic acid (GAA). The obtained solutions were dried at 200 degree celcius in air to form gel structure of KLTO mixture and heat treated at 850 degree celcius for 3 hours in air. After the sintering, the powders were dispersed in propionic acid and the obtained suspensions were deposited on Si substrates using spin coating system and then annealed at 1000 degree celcius for 5 hours in air. Thermal, structural, microstructural, mechanical properties of the coatings were characterized through differential thermal analysis-thermogravimetry (DTA-TG), Fourier transform infrared (FTIR), X-ray diffraction (XRD), scanning electron microscopy-energy dispersive spectroscopy (SEM-EDS), surface profilometer, nanoindenter and scratch test devices. Methylene blue photocatalytic performance experiments were carried out in a solar box which is simulating natural radiation and ultraviolet-visible (UV-Vis) absorption spectra. According to the measurement results of K2*Ln*2Ti3O10 (Ln; La, Nd, Gd, Sm, Dy) samples, K2La1.5Sm0.5Ti3O10, exhibit the highest photocatalytic activity.

Keywords: Photocatalytic activity, sol-gel technique, layered perovskite, K2*Ln*2Ti3O10, methylene blue

NADİR TOPRAK ELEMENTİ KATKILI YENİ NESİL $K_2Ln_2Ti_3O_{10}$ YARI İLETKEN FİLMLERİN SENTEZLENMESİNİN DİZAYNI VE ENDÜSTRİYEL UYGULAMALARI

ÖZ

Bu çalışmada fotokatalitik uygulamalar için K2*Ln*2Ti3O10 (Ln; La, Nd, Gd, Sm, Dy) ince filmlerin sentezlenmesi ve karakterizasyonu araştırılmıştır. Tabakalı perovskit yapılar sol gel metoduyla üretilmiştir. Bu amaç doğrultusunda, K, Ti, La, Nd, Gd, Sm ve Dy tabanlı başlangıç maddeleri propiyonik asit ve glasiyal asetik asit (GAA) kullanarak saydam çözeltiler elde edilmiştir. Elde edilen solusyonlar hava ortamında 200 santigrad derecede kurutulmuş ardından 850 santigrad derecede üç saat boyunca ısıl işleme tabi tutulmuştur. Sinterleme aşamasından sonra elde edilen tozlar propiyonik asitte disperse edilerek Si altlıklar üzerine döndürme kaplama yöntemiyle kaplanmıştır. 1000 santigrad derecede 5 saat boyunca tavlama işleminin ardından ince filmler hazırlanmıştır. Kaplamaların termal, yapısal, mikroyapısal ve mekanik özellikleri DTA-TG, FTIR, XRD, SEM ve kazımalı test cihazlarıyla belirlenmiştir. Metilen mavisi ile yapılan fotokatalitik deneylerde doğal radyasyon simule edilerek üretilen sun test cihazı ve (UV-Vis) spektra kullanılmıştır. K2*Ln*2Ti3O10 (Ln; La, Nd, Gd, Sm, Dy) ile yapılan deneylerde elde edilen sonuçlara göre, K2La1.5Sm0.5Ti3O10en yüksek fotokatalitik aktiviteyi göstermiştir

Anahtar kelimeler: Fotokatalitik aktivite, sol-jel teknik, tabakalı perovskit K2*Ln*2Ti3O10, metilen mavisi

CONTENTS

Page

LIST OF FIGURES

Page

LIST OF TABLES

Page

CHAPTER ONE
INTRODUCTION

Hydrogen is an extremely valuable chemical commodity, not only in today's industrial marketplace, but even more so in the emerging Green Economies so vital to the future of our planet and its people. Green futures will need to rely less-and-lesson fossil fuels, and more-and-more on solar, wind, biomass, geothermal, and other renewable energy resources. Hydrogen is envisioned as one of the primary media for the storage and distribution of energy derived from this renewable portfolio. To achieve the vision, much work is needed in the development of new more practical technologies and infrastructures for hydrogen production, storage, delivery, and utilization. Nonpolluting technologies for large-scale hydrogen-production utilizing renewable energy are of particular importance. Among the viable renewable hydrogen-production approaches, solar options, particularly solar-powered water-splitting, offer the best hope for large-scale renewable production with low carbon emissions. Several solar-to-hydrogen (STH) pathways are possible, including solar electrolysis, where electricity generated by photovoltaic (PV) or concentrated solar thermal (CST) power plants is used to drive electrolyzer systems, for example, commercial "alkaline" or "PEM" electrolyzers.

Among a number of alternative, more direct conversion pathways, photoelectrochemical (PEC) water-splitting using semiconductor photoelectrodes or photocatalysts remains one of the most promising, though still elusive based on challenges in developing stable and efficient PEC materials, devices, and systems. Broadly speaking, a PEC system combines the harnessing of solar energy and the electrolysis of water into a single conversion system. As illustrated in Figure 1.1 sunlight shining on a suitable PEC semiconductor device immersed in a water-based solution can simultaneously drive water oxidation and hydrogen reduction electrochemical reactions to split water. This process evolves hydrogen and oxygen gases, effectively converting the solar energy in to stored chemical energy.

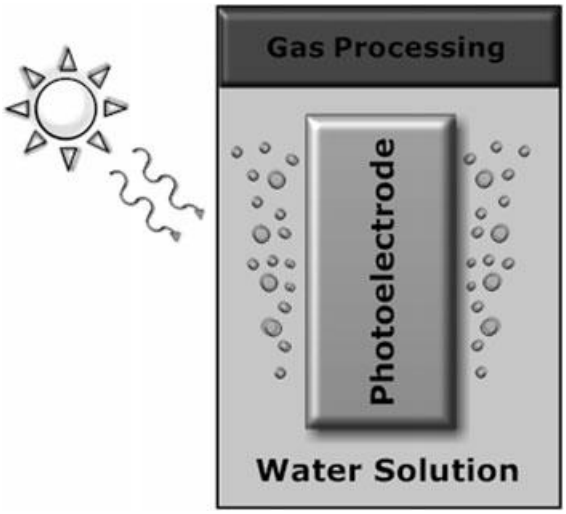

Figure 1.1 A PEC photosensitive electrode uses sunlight to split water, evolving hydrogen and oxygen gases from solution (Miller, DeAngelis & Mallory, 2012).

The PEC approach is simple and elegant in concept, but is challenging to implement in practice since it relies on complex interactions involving sunlight, semiconductors, and liquid solutions. In a practical system, the semiconductor material must efficiently absorb sunlight and generate sufficient photovoltage to split water, while the semiconductor interface must be favorable to sustaining the hydrogen- and oxygen-gas evolution reactions. In addition, the PEC system needs to remain stable in solution, and must be inexpensive for compatibility with large scale deployment (Miller, DeAngelis & Mallory, 2012).

The Honda–Fujishima effect of water splitting using a TiO_2 electrode was reported in the early 1970s. When TiO_2 is irradiated with UV light electrons and holes are generated. The photogenerated electrons reduce water to form H_2 on a Pt counter electrode while holes oxidize water to form O_2 on the TiO_2 electrode with some external bias by a power supply or pH difference between a catholyte and an anolyte. Numerous researchers had extensively studied water splitting using semiconductor photoelectrodes and photocatalysts since the finding. It has been recently reported that perovskite type layered several materials are more photoactive than TiO_2. Literature researches on lanthan-titanates which is one of the layered structures continue. Inasmuch as lanthan-titanates ($K_2La_2Ti_3O_{10}$) in perovskite

structure are more active than TiO_2, this topic has been increasingly investigated with a big interest.

Yang et. al. (2007) prepared layered perovskite type oxide $K_2La_2Ti_3O_{10}$ powders under air, Ar and H_2 calcination atmospheres by sol-gel method and characterized by X-ray diffractometry, UV-Vis diffuse reflectance and X-ray photoelectron spectroscopy. The influence of the calcination atmosphere on the photocatalytic reactivity of $K_2La_2Ti_3O_{10}$ for hydrogen production was investigated. The photocatalytic reactivity of $K_2La_2Ti_3O_{10}$ prepared under air, Ar and H_2 atmospheres was compared with that prepared under ultraviolet and visible light radiation using I^- as electronic donor. The results show that $K_2La_2Ti_3O_{10}$ prepared under Ar and H_2 atmospheres has higher photocatalytic activity for hydrogen production than that prepared under air atmosphere.

Wu et al. (2008) synthesized the layered perovskite, $K_2La_2Ti_3O_{10}$ photocatalysts by soft hydrothermal method and contrasted with preparing by conventional solid state reaction method. The photocatalysts prepared by hydrothermal technique had a higher photocatalytic activity than that prepared by conventional solid state reaction method.

Yang et. al. (2009) synthesized the layered perovskite type oxides, $K_2La_2Ti_3O_{10}$ and zinc (Zn)-doped $K_2La_2Ti_3O_{10}$ were prepared by sol–gel method and were characterized by power X-ray diffraction, UV–vis diffuse reflectance and X-ray photoelectron spectroscopy. The photocatalytic activity for water splitting of the catalyst powders was investigated with I^- as electron donor under ultraviolet and visible light irradiation respectively. The electronic structure of the powders has been analyzed by the first principles calculation, which reveals the photo responses in the visible region and the improvement of the photocatalytic activity of $K_2La_2Ti_3O_{10}$. Conclusions were made that zinc (Zn)-doped $K_2La_2Ti_3O_{10}$ exhibited higher reactivity for hydrogen production.

Uma et. al. (2011) achieved noticeable lowering of the energy gaps for the layered perovskite $K_2La_2Ti_3O_{10}$ as a result of the attempts made to incorporate Sn^{2+} and N^{3-} ions. Incorporation of Sn^{2+} ions was carried out by the ion-exchange reaction of $K_2La_2Ti_3O_{10}$ with aqueous tin (II) chloride solution. Nitrogen incorporation was attempted by the solid state reaction of the parent oxide with urea around 400 ^oC in air. The resultant oxides have been characterized by power X-ray diffraction, UV–visible diffuse reflectance spectroscopy, and Fourier transform infrared spectroscopy. The product oxides obtained as a result of cation and anion intended substitutional studies have been found to be useful for the visible light photocatalytic decomposition of organic dyes such as rhodamine B.

Liang et. al. (2012) synthesized a series of cadmium sulfide (CdS)-sensitized layered perovskite-type compound ($K_2La_2Ti_3O_{10}$) photocatalysts by loading CdS particles on $K_2La_2Ti_3O_{10}$ via a facile precipitation method. The photocatalysts were characterized by X-ray diffraction, X-ray photoelectron spectroscopy, and ultraviolet–visible (UV–vis) diffuse reflection spectra. The photocatalytic activities of these catalysts for H_2 production were investigated in the presence of a Na_2S sacrificial reagent under visible light irradiation. The results revealed that the CdS/ $K_2La_2Ti_3O_{10}$ samples displayed a strong light absorption in the visible region, and the UV–vis diffuse reflectance spectra changed with the proportion of CdS present. This enhanced photocatalytic activity can be attributed to the efficient separation of electron–hole pairs and prevention of their recombination under the joint effects of the electric field established at the heterojunction and the layered space of $K_2La_2Ti_3O_{10}$.

This thesis is structured around the synthesis, characterization, and photocatalytic activity of $K_2Ln_2Ti_3O_{10}$ (Ln= Nd, Gd, Sm, Dy) thin films that produced by using sol-gel technique for photocatalytic applications specifically degradation of methylene blue dye. The solutions were spin coated on the Si(100) substrates. Solution characterization were performed by measuring turbidity, pH, contact angle and viscosity of solutions. In order to use suitable process regime, define chemical structure and reaction type of intermediate temperature products, Differential

Thermal Analysis-Thermogravimetry (DTA-TG) and Fourier Transform Infrarared (FTIR) devices were used in the film production. Structural analysis of the produced films was performed by using multipurpose X-Ray Diffraction (XRD) and surface morphology was investigated using Scanning Electron Microscope (SEM). Adhesion properties of thin films were determined by scratch tester. The photocatalytic activities of $K_2Ln_2Ti_3O_{10}$ (Ln= Nd, Gd, Sm, Dy) thin films for methylene blue degradation were investigated under visible light irradiation.

CHAPTER TWO
THEORETICAL BACKGROUND

2.1 Basic Mechanism of Photocatalysis

The conversion of solar energy via photocatalytic reactions that occur on the surface of semiconductor materials has been extensively investigated ever since the pioneer work of Fujishima and Honda on using TiO_2 photoanode for photochemical water splitting. Photocatalysis has been considered as a promising approach for the sustainable organic pollutants decomposition in water and air, which has been already used in some practical applications. Regardless of the different reactions occur on the semiconductor surface, the basic mechanism for all the photocatalytic reactions is essentially the same. Fundamentally, photocatalytic reactions involve the following steps shown in Figure 2.1. (1) Light energy is absorbed by the photocatalyst. If the incident light energy is equivalent to or higher than the band-gap of the semiconductor, electrons can receive energy from the photons and are excited from the valence band to the conduction band, leaving free holes in the valence band. (2) The photo-generated electrons and holes (charge carriers) may recombine either in bulk or on surface of semiconductor within a very short time, releasing energy in the form of heat or photons. However, if the electrons and holes are lucky enough, they could migrate to the surfaces of the semiconductor particles. (3) The free electrons can subsequently undergo reduction reactions with electron acceptors adsorbed by the surface of semiconductor, whereas the holes can directly oxidize adsorbed molecules or react with surface hydroxyl groups to produce hydroxyl radicals which are strong oxidizing agents. These oxidation and reduction processes together with some subsequent secondary reactions are the basic mechanisms of photocatalytic process, which underpin the development of a number of very important photocatalytic applications including organic pollutant decomposition (oxidation process by holes) for water and air purifications, water splitting and CO_2 conversion (Wang & Zong, 2014).

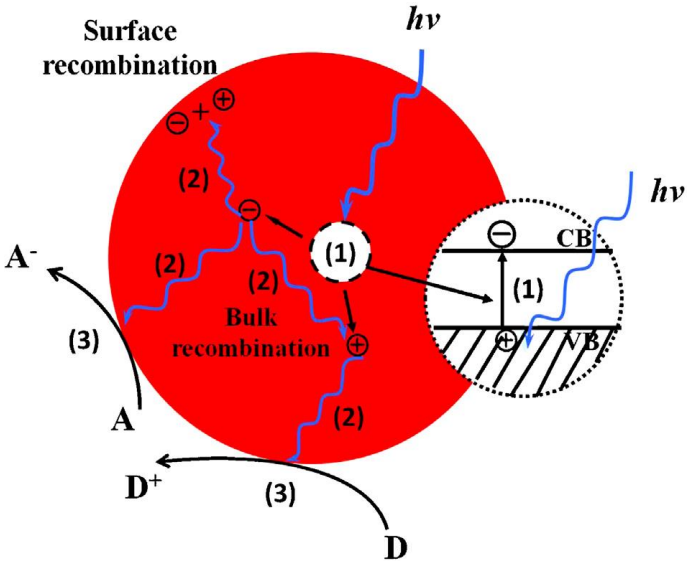

Figure 2.1 Schematic steps for photocatalytic reactions that occur on semiconductor surface. (Wang & Zong, 2014)

If charge separation is maintained, the electron and hole may migrate to catalyst surface where they participate in redox reactions with sorbed species. Specially, h^{+}_{vb} may react with surface-bound H_2O or OH^- to produce the hydroxyl radical and e^-_{cb} is picked up by oxygen to generate superoxide radical anion ($O_2^{\cdot-}$), as indicated in the following Equations 2.1- 2.

absorption of efficient photons by semiconductor

$$\text{Semiconductor} + h\nu \rightarrow e^-_{cb} + h^+_{vb} \quad (2.1)$$

formation of superoxide radical anion

$$O_2 + e^-_{cb} \rightarrow O_2^{\cdot-} \quad (2.2)$$

neutralization of OH group into $^{\cdot}OH$ by the hole

$$(H_2O \Leftrightarrow H_+ + OH^-)_{ads} + h_{vb+} \rightarrow {}^{\cdot}OH + H_+ \quad (2.3)$$

It has been suggested that the hydroxyl radical (.OH) and superoxide radical anions ($O_2^{\cdot-}$) are the primary oxidizing species in the photocatalytic oxidation processes. These oxidative reactions would results in the degradation of the pollutants as shown in the following Equations 2.4 - 2.5;

oxidation of the organic pollutants via successive attack by OH radicals

$$R + {}^{\cdot}OH \rightarrow R'^{\cdot} + H_2O \quad (2.4)$$

or by direct reaction with holes

$$R + h^+ \rightarrow R^{\cdot +} \rightarrow \text{degradation products} \quad (2.5)$$

(Muneer et. al., 2003)

2.2 Fundamental Requirements for a Semiconductor Photocatalyst

The photocatalytic properties of a semiconductor depend strongly on the electronics of the band structure. In an ideal semiconductor photocatalytic process, as illustrated in Figure 2.2 absorption of light higher in energy than the semiconductor's band gap creates an electron/hole pair, where electrons are excited from the valence band (VB) to the conduction-band (CB), thus creating holes in the VB.

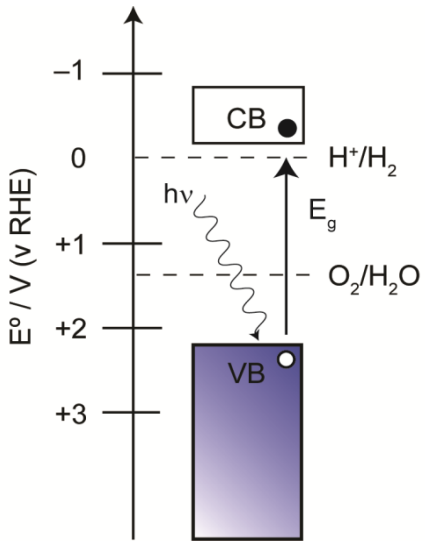

Figure 2.2 Ideal band structure for a semiconductor water splitting photocatalyst (Breault, 2013)

Four fundamental requirements for an efficient semiconductor photocatalyst are necessary for photocatalytic water splitting to proceed efficiently. First, in order to maximize absorbing longer wavelengths of the solar spectrum, the band gap should be ~ 2 eV, which corresponds to absorption of wavelengths less than ~ 620 nm and accounts for any associated overpotential. Traditionally, many wide band gap semiconductors, such as TiO_2 and $SrTiO_3$, have been explored as water splitting

photocatalysts; however, their efficiencies are limited by their band gaps (≥ 3.0 eV), which corresponds to UV light absorption only.

The drawback for UV active catalysts relates to the solar flux density, N_{ph}, in the UV and visible regions of the solar spectrum, shown in Figure 2.3. The solar spectrum is comprised of 2 % UV light ($\lambda < 400$ nm, $N_{ph} = 8.4 \times 10_{19}$ m^{-2} s^{-1}) compared to 47 % visible light ($400 < \lambda < 800$ nm, $N_{ph} = 1.6 \times 10_{21}$ m^{-2} s^{-1}) highlighted in grey in Figure 2.3. Approaches to modifying semiconductors to absorb longer wavelengths of light has been the subject of much research in order to maximize efficiency by absorbing light throughout the solar spectrum.

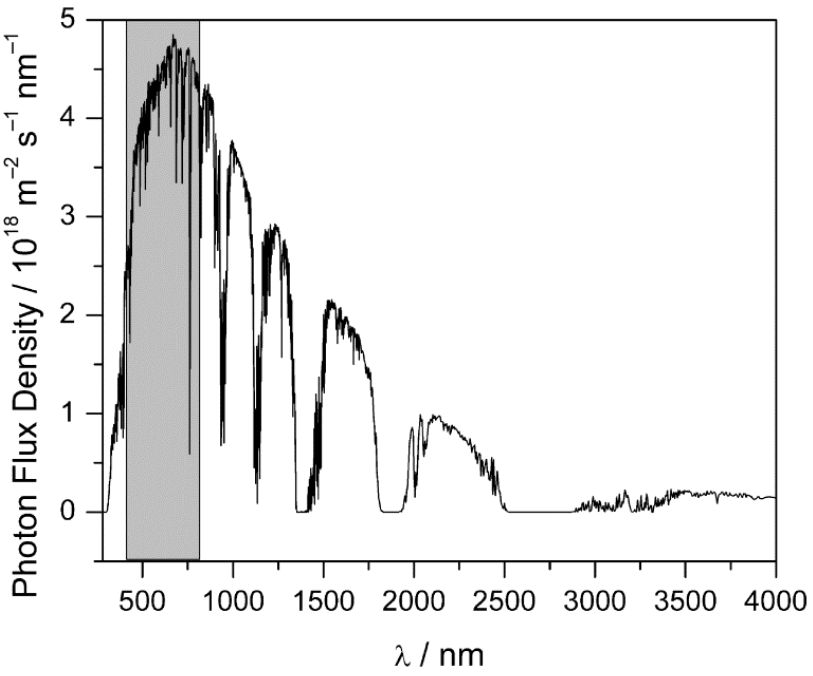

Figure 2.3 Photon flux density at various wavelengths of the solar spectrum (Breault, 2013)

Second, when targeting overall water splitting the band edge energies should straddle the water splitting half reactions, as illustrated in Figure 2.2. Upon irradiating a semiconductor and creating electron/hole pairs, the electrons and holes must be at sufficient energies in order for both half reactions to occur. The CB should be at an energy more negative than the proton reduction potential (0 V vs. NHE under standard conditions), and the VB energy should be more positive than

the water oxidation potential (1.23 V vs. NHE under standard conditions) in order for overall water splitting to occur on a single semiconductor.

Furthermore, upon irradiating the photocatalyst, generating charge-carriers that subsequently migrate to surface reaction sites must occur rapidly with respect to recombination in the bulk of the material. Highly crystalline materials are attractive for suppressing recombination occurring at defect sites and grain boundaries simply because fewer defects exist.

Finally, the material must be chemically stable in the presence of reactive, oxidizing species. There are many attractive candidates with narrow band gaps for the overall water splitting reaction; however, the stability of some compounds, such as CdS and WO_3, limits their wide scale use. The degradation of these catalysts is caused by photogenerated holes degrading the compound in addition to oxidizing water (Breault, 2013).

2.3 Photocatalyst for Water Splitting

In the last decade, many different materials for photocatalytic water splitting have been prepared, and the main challenges, including broad absorption capability and reduced recombination probability, have been identified to synthesize a good material for photocatalytic water splitting by research groups all over the world (Marschall & Wang, 2013).

Figure 2.4 shows elements constructing heterogeneous photocatalyst materials. The elements are classified into four groups; (i) to construct crystal structure and energy structure, (ii) to construct crystal structure but not energy structure, (iii) to form impurity levels as dopants and (iv) to be used as cocatalysts. Most metal oxide, sulfide and nitride photocatalysts consist of metal cations with d^0 and d^{10} configurations. Their conduction bands for the d^0 and d^{10} metal oxide photocatalysts are usually composed of d and sp orbitals, respectively, while their valence bands consist of O 2p orbitals (Kudo & Miseki , 2009).

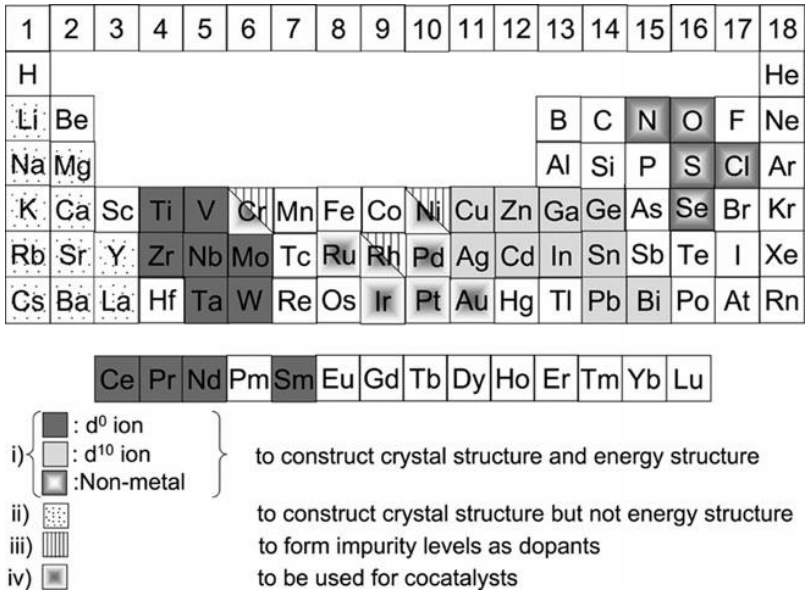

Figure 2.4 Elements constructing heterogeneous photocatalysts (Kudo & Miseki, 2009)

Many mixed metal oxides with early transition metal ions having d^0 configuration (Ti^{4+}, Nb^{5+}, Ta^{5+}) have been explored. Specifically, several of the layered perovskites such as $K_2La_2Ti_3O_{10}$, $RbPb_2Nb_3O_{10}$, $KLaNb_2O_7$, have been identified as photocatalysts in the presence of co-catalysts (Pt, NiO, etc.) for the evolution of H_2 from water under UV light radiation. These layered oxides are attractive photocatalytic materials for the following reasons: (i) their structures consist of two dimensional perovskite slabs interleaved with cations and this structural type is expected to increase the lifetime of the photogenerated electrons and holes, and thereby increasing the efficiency of the materials; (ii) the perovskite slabs are normally made up of metals such as Ti, Nb, or Ta, that have been preferred as photocatalysts under UV irradiation; (iii) numerous low temperature synthetic possibilities exist to study the influence of cationic and/or anionic substitutions by the appropriate tuning of the band gaps (Uma et al. , 2011).

2.3.1 Structure of $K_2La_2Ti_3O_{10}$

$K_2La_2Ti_3O_{10}$ is an n-type semiconductor layered compound consisting of negatively charge lanthanum titanate perovskite layers and interlayer K^+ ions as shown in Figure 2.5. The adjacent triple perovskite sheets, $La_2Ti_3O_{10}$, are stacked

with a displacement of 1/2 along the (110) direction. A lanthanum ion occupies the 12-fold site in the center of the perovskite lattice. According to the X-ray diffraction data, the cell parameters $K_2La_2Ti_3O_{10}$ are a = b = 0.387 nm, c = 2.98 nm, face distance (001) = 1.49 nm, and thick of $La_2Ti_3O_{10}^{2-}$ is 1.19 nm. The interlayers are bonded by static force. Due to the weaker combination between the interlayers, $K_2La_2Ti_3O_{10}$ can readily exchange its intercalation ion and expand (Wun et al., 2010)

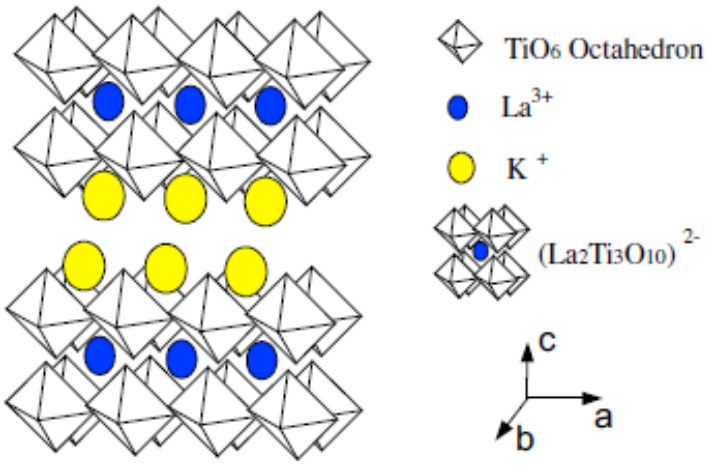

Figure 2.5 Schematic structure of $K_2La_2Ti_3O_{10}$ (Li et al., 2010)

Layered oxides with perovskite related structures have the general formula $A_m[A'_{n-1}B_nO_{3n+1}]$, where $A'_{n-1}B_nO_{3n+1}$ is the perovskite strata, A is an interlayer cation usually an alkali metal, B is a transition metal and A' is an alkaline or rare earth metal. When m = 2 the phase is called a Ruddlesden-Popper layered perovskite. Traditionally these materials are prepared by high temperature ceramic methods. In terms of chemical reactivity, it has been shown that the interlayer cations can be exchanged with other cations or cationic units by low temperature, topochemical reactions. Low temperatures (T < 500 ^oC) offer the potential for making new compounds with targeted properties. Topochemical reactions are driven by the crystal structure rather than by the chemical nature of the reactants. In this manner, the basic crystal structure of the parent phase remains the same, except for the corresponding changes in the lattice parameters necessary to accommodate the new species. Topochemical methods include ion exchange, intercalation/deintercalation,

exfoliation and dehydration/condensation reactions. These methods provide access to a wide variety of metastable phases that cannot be formed by traditional solid-state reactions (Neiner, 2005).

The interest in these compounds has increased since the discovery that the interlayer space alkali cations can be replaced with other cations or cationic units while maintaining the layered perovskite structure. When the monovalent alkali metals are replaced with divalent ions or cationic units, in order for the charge balance to be maintained, one divalent unit replaces two monovalent ions. Therefore, the interlayer space in the ion exchanged product has empty sites. On these empty sites, an alkali metal can be inserted.

One special feature of ion-exchangeable materials related with photocatalysis is their spatially separately photocatalytic oxidative and reductive reaction sites (Wang & Zong, 2014). Takata et al. investigated a series of ion-exchangeable layered perovskite type materials with high efficiency for overall water splitting reactions (Domen et al., 1997). They proposed that O_2 evolution occurred at the interlayer space of the layered materials while H_2 evolution occurred at the external surface.

2.4 Sol- Gel Process

2.4.1 The Chemistry of Precursors Solution

If inorganic sols and gels can be obtained by various methods, they are often directly synthesized from chemical reactants dissolved in a liquid medium. The chemical reactants which contain the cation M (metal) present in the final inorganic sol or gel is called the chemical precursor. Its chemical transformations are complex and involve a competition at the molecular level between the reaction responsible for the formation of open structures and the one leading to dense solid. Those same reactions are responsible for the controlled dispersion of dense colloidal particles in a sol or their agglomeration into a gel (Pierre, 1998).

All types of precursors can be used, provided they are miscible. For thin film production metal alkoxides are better than its salts as a precursor to achieve crack-free, pinhole-free, homogeneous and textured films.

Solvents which dissolve precursor have a molecular structure chracterized both by a permanent dipole moment μ and by a relative dielectric constant ε_r. A high relative dielectric constant ($\varepsilon_r > 40$) is often due to the existance of a permanent dipole moment. Such molecules have good ionizing properties and can therefore dissolve other polar solute. On the other hand when the solvent's relative constant is low ($\varepsilon_r < 20$), it has a weak ionizing property and can only dissolve less polar solute.

Sol-gel precursors undergo chemical reaction with solvents and the other species present in the solution. One of the most efficient models used to predict those reactions is the Partial Charge Model. Various atomic or molecular groups called ligands can bind to a complex C or cation M either directly or by substituting another ligand. The mechanism of the transformation depends on the partial charge of the different atoms in the species. Those with a negative partial charge are nucleophilic, and those with a positive charge are electrophilic. Similarly, in a substitution reaction, the new ligands with the highest partial charge are the nucleophile while the group in the metal complex with the highest positive charge is the leaving group (Erol, 2009).

2.4.2 Hydrolysis and Condensation Reaction

Hydrolysis can be denoted by deprotonation of a solvated M cation and it consists in the loss of a proton by one or more of the water molecules that surrounds the M in the first solvatation shell. As a consequence, the aquo ligand molecule, H_2O that is bonded to the metal is either transformed into an hydroxo ligand, OH^-, if only one proton leaves, or into an oxo ligand O^{-2}, if two protons detaches.

After hydrolysis, condensation reaction occurs to form a polynuclear complex consisting of two metal atoms. Condensation, in aqueous solutions, is the result of

either an olation or an oxolation reaction. In either case, one must be quite careful as the oxygen present sometimes speeds the reaction to apoint where it becomes necessary to work in the the neutral atmosphere of argon in order to control it. In the first case, transfer of the H to an OR ligand according to the reaction below (olation process);

$$-M-OH- \; + \; -M-OR- \; \rightarrow M-O-M+ROH \tag{2.6}$$

In oxolation case, an oxo bridge (-O-) is formed between two metal centers according to Reaction (2.7);

$$-M-OH \; + \; -M-OH \; \rightarrow M-O-M+ROR \tag{2.7}$$

As mentioned above in the Reactions 2.6 and 2.7 the same reactions can be written for K, La, and Ti based precursors. Both hydrolysis and condensation keep on going thus gradually building up a tridimensional network that, at the end, often forms a solid phase. This process is accelerated by heat as the rate of the both reactions increases together with the temperature. Since the kinetics of hydrolysis and condensation, and hence the overall reaction and the type of polymers formed, depends on the pH, a great variety of materials with different structures can be obtained. These include linear polymers as well as dense colloidal particles and smaller ones with more or less weakly bonded cross-linked clusters of polymers (Pierre, 1998).

2.4.3 Thermodynamics of Nucleation and Crystal Growth

The chemical reactions which transform a precursor solution, produce a large variety of complexes. The formation of solid particles can be described as a process of nucleation and growth, according to the sequence (2.8);

$$\text{hydrolysis} \rightarrow \text{condensation} \rightarrow \text{nucleation} \rightarrow \text{growth} \tag{2.8}$$

The transformation from the amorphous to the crystalline state can be considered with phenomenological thermodynamics. The most favorable site for the nucleation can be derived by classical nucleation theory. It should be noted that much of the volume is not far from the surface and the interface with the substrate and heterogeneous nucleation is more likely to occur in the thin films. Assuming for simplicity that regions of crystalline KLTO is spherical with a radius r, a free energy change ΔG, due to homogeneous nucleation is given by

$$\Delta G = 4\pi r^2\gamma + \frac{4}{3}\pi r^3 + \Delta G_V \tag{2.9}$$

where γ is the interfacial energy between the amorphous and the crystalline KLTO and ΔGv the free energy change per unit volume. In case of solid-solid transformation, a nucleus usually undergoes distortion in atomic arrangement as a result of contact with surrounding matrix and/or the substrates. Consequently, a distortion energy term must be added in a right-hand side of Equation 2.9. In the present case however, both the matrix and the substrate are amorphous giving incoherent interfaces, and the nucleus is not affected by them in terms of the atomic arrangement. Therefore, the distortion energy can be regarded as zero (Fujihara et al., 2001). From the nucleation $\partial(\Delta G)/\partial_r=0$, a free energy barrier, ΔG_c, which subcritical embryos must overcome to become supercritical nuclei, is derived as follows in Equation 2.10

$$\Delta G_c = \frac{16\,\pi\gamma}{3(\Delta G_V)^2} \tag{2.10}$$

At the substrate surface, "amorphous KLTO" has a higher interfacial energy than crystalline KLTO. When the nucleus forms on substrate, some high-energy substrate/amorphous, KLTO surfaces are replaced by lower-energy substrate/nucleus surface. This contributes to a smaller overall interfacial energy in Equation 2.10, resulting in reduction of the free energy barrier. Thus, the heterogeneous nucleation at the substrate surface is more likely to occur. Consideration of a polyhedron nucleus leads to a similar tendency. When the nucleus is formed on a flat substrate characterized by contact angle, θ, the reduced barrier, ΔG^*_c, can be expressed by:

$$\Delta G_c^* = f(\theta)\Delta G_c \tag{2.11}$$

where

$$f(\theta) = {}^1/_4\,(2 + cos\theta)(1 - \cos\theta)^2 \tag{2.12}$$

The θ value is determined by the surface energy of the substrate (γ_s) and the nucleus (γ_n) and the interfacial energy between them (γ_{sn}) :

$$cos\theta = \frac{\gamma_s - \gamma_{sn}}{\gamma_s} \tag{2.13}$$

Figure 2.6 shows a relationship between f(θ) and θ. The f(θ) value increasing the contact angle θ. Therefore ΔG^*_c in Equation 2.11 is lower with smaller contact angle of the nucleus. $\gamma_s=\gamma_n$ and $\gamma_s=0$ in homoepitaxial systems give cosθ=1, f(θ)=0, and accordingly $\Delta G^*_c = 0$. On the other extreme, $\gamma_{sn}= \gamma_s+\gamma_n$ gives $\Delta G^*_c = \Delta G_c$, where the homogeneous nucleation occurs without the effect of the substrate.

γ_{sn} is generally less than the sum of γ_s and γ_n. When γ_s is constant as for the glass substrates, γ_n is determined by γ_n as follows:

$$\gamma_{sn} = \alpha\gamma_n \qquad 0 < \alpha < 1 \tag{2.14}$$

From Equations 2.14 and 2.15,

$$cos\theta = \left(\frac{\gamma_s}{\gamma_n}\right) - \alpha \tag{2.15}$$

that α is constant, the lowest γ_n gives the largest cosθ and hence, the smallest ΔG^*_c

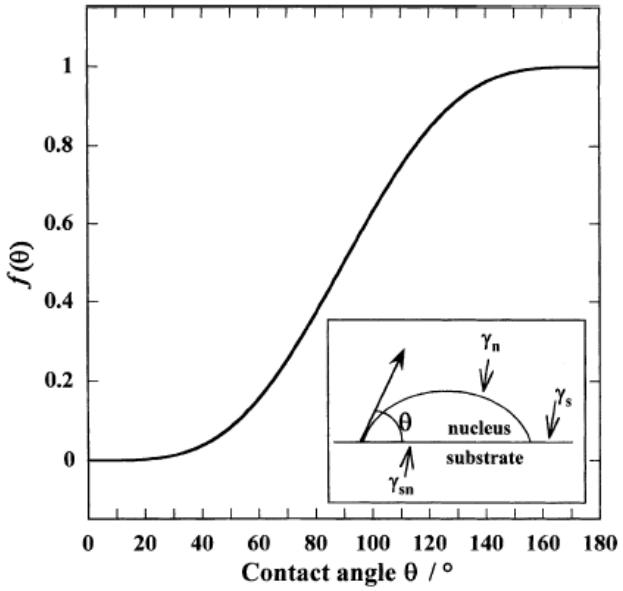

Figure 2.6 A relationship between f(θ) and contact angle, θ (Pierre, 1998).

Eventually, we can presume reason for the random orientation often observed in the sol-gel derived KLTO thin films. The rate of the heterogeneous nucleation typically reaches a maximum at a lower temperature. The homogeneous nucleation competes with the heterogeneous one at higher temperatures. This limits the annealing of the films to lower temperatures. On the other hand, the driving force for the crystallization is higher at lower temperatures because of a larger difference between the melting point and the nucleation temperature.

2.4.4 Gelation

The process in which a three-dimensional network is formed through linking together of sol cluster is called gelation. Gelation occurs when the extent of polymerization reactions ξ reaches a critical value ξ_c. This precise critical stage, when for the first time a polymer of infinite size is formed by comparison with the molecular scale, defines the gel point. In a practical manner, at this point the product resulting from polymeric condensations transforms suddenly from a viscous liquid to a material with elastic properties.

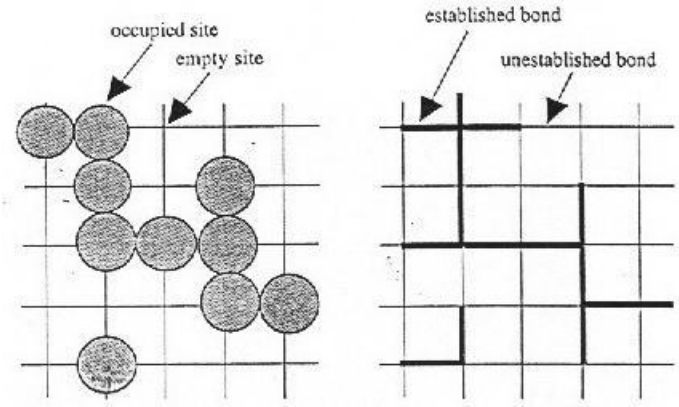

Figure 2.7 (a) Site percolation and (b) bond percolation on a square bi-dimensional network (Pierre, 1998).

Gelation can be described as the frame work of critical phenomena in thermodynamics in particular by the percolation theories. The most simple of the percolation models is isotropic such as the bond percolation and the site percolation (Figure 2.7). In these models, either a bond is established or a site is occupied with probability p, in a completely random fashion throughout a geometrical network. Another critical parameter is the percolation threshold probability p_c as shown in Figure 2.8. However, its value depends on the coordination number Z in the case of a regular site network or on the volume fraction ϕ occupied by the sites if they are replaced by hard spheres packed in a random fashion. Critical probability P_c is related to the coordination number Z by

$$P_c = \xi_c = \frac{1}{z-1} \tag{2.16}$$

Its main default is to neglect the formation of closed loops contrary to what occurs in real gelation.

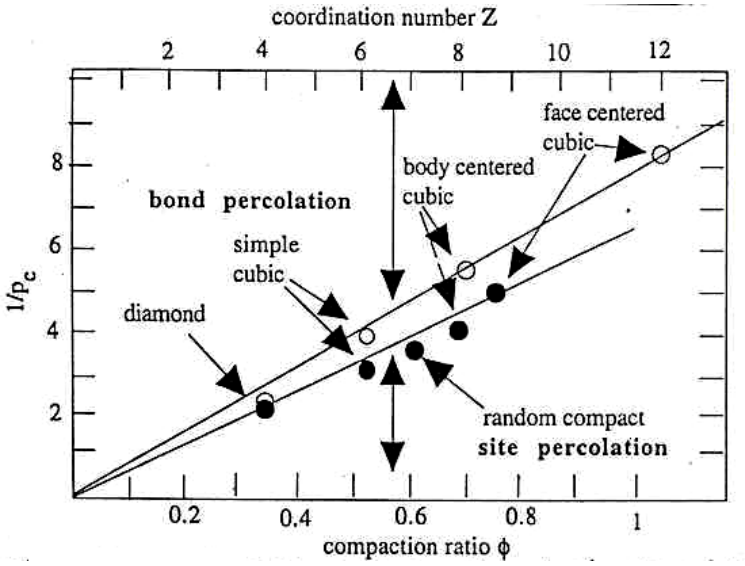

Figure 2.8 Empirical correlation between the percolation threshold and the lattice (Pierre, 1998)

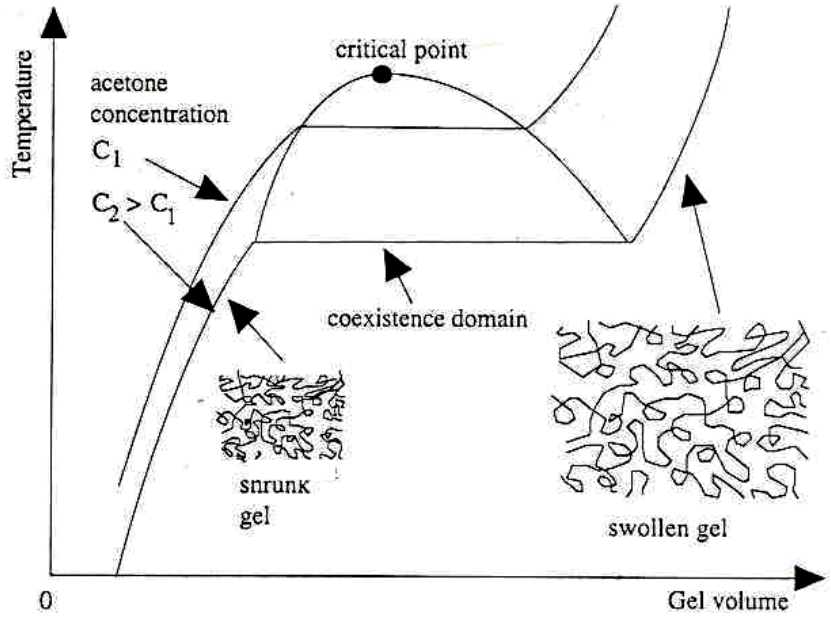

Figure 2.9 State diagram of an organic polymer gel (Pierre, 1998).

The molecular groups that form the solid network of a gel can present a more or less strong affinity for molecules in the liquid which impregnates them. This affinity can be strong enough, in some cases, to overcome the mechanical strength of the network without destroying it. That is to say, the gel swells or shrinks and in some gels such as organic polymeric gels, this change in gel volume is reversible. A

polymeric gel can practically adapt one of two possible states: a shrunken state and a swollen state. These two states can coexist, exactly as a liquid and a gas state can coexist in a classical liquid-gas phase transformation. Moreover, a critical point exists above which the gel passes gradually from one state to the other. Below the critical point is possible to obtain either one of these two states; or the coexistence of both, as in classical liquid-gas state transition. The critical point corresponds to critical conditions where the compressibility of the gel network becomes infinite; this is a true critical point in a thermodynamic sense. Overall, the state transition of a covalent polymeric gel network can be described within the theory of critical phenomena, and a state diagram can be drawn as shown in Figure 2.9.

2.4.5 Drying

Drying rate per unit area of gels follows two successive regimes: a "constant-rate" period, followed by a "falling-rate" period (Figure 2.10 curves a and b).

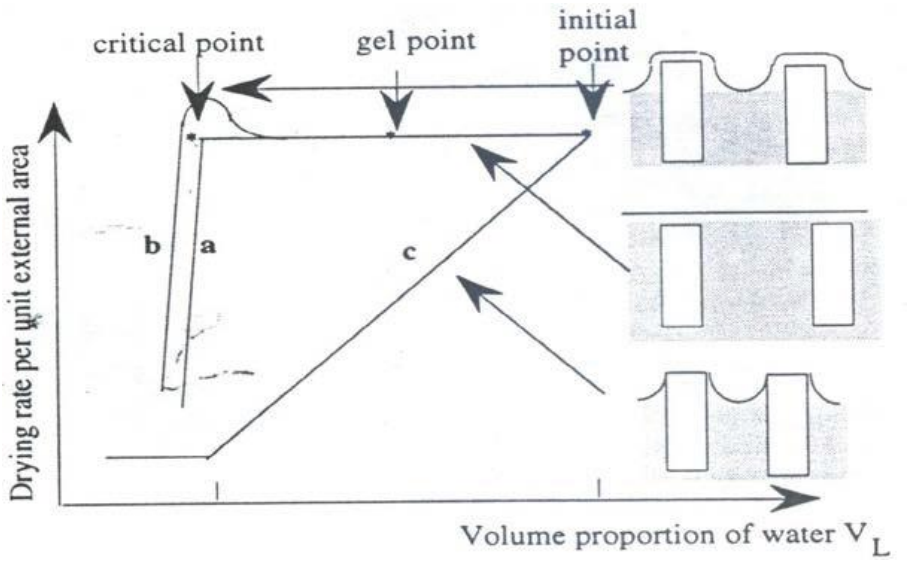

Figure 2.10 Evolution of the drying-rate per external unit area of wet gel as a function of the liquid volume proportion VL: (a) and (b) experimental graphs; (c) graph if the drying rate was proportional to the relative surface of menisci (Pierre, 1998).

The transition between these two regimes occurs at a very sharp point named the "critical-point". Drying is irreversible transformation of the gel which is composed

of a solid network and liquid matrix.The capillary mechanism explain wellthe reproducible adsorption hysteresis curves of water in silica gels. This mechanism can be summarized as follows:

1) Evaporation creates a liquid vapor meniscus at the exit of pores in the gel.

2) This induces a hydrostatic tension in the liquid, which is balanced by an axial compression on the solid.

3) The latter compression makes the gel shrink.

4) As a result of shrinkage, more liquid is fed to the menisci at the exit of the gel pores, where it is evaporated and so on.

2.4.6 Sintering

The specific surface area of the porosity is an evolution named sintering. Sol-gel ceramics just after drying and even after heat treatments at intermediate temperatures often have a very high specific surface area and an extremely small grain size. Since states with a lower Gibbs free energy are more stable at a given temperature and pressure, the specific surface area should tend to decrease, an evaluation which can proceed according to two types of pore evaluation: (a) by changing the shape of pores but not their volume and (b) by eliminating the pores. Hence, the dense materials can be obtained after the sintering process (Pierre, 1998).

CHAPTER THREE
EXPERIMENTAL STUDIES

3.1 Aim of Thesis

The objective of this study was to fabricate $K_2Ln_2Ti_3O_{10}$ (Ln= Nd, Gd, Sm, Dy) thin films using sol-gel technique for photocatalytic applications. With this aim, solutions to produce $K_2Ln_2Ti_3O_{10}$ (Ln= Nd, Gd, Sm, Dy) thin films including K, La, Nd, Gd, Sm, Dy and Ti based precursors, solvent and chelating agent were prepared.

In order to determine solution characteristics which affect thin film structure; turbidity, pH values and rheological properties of the prepared solutions were measured by turbidimeter, pH meter and rheometer machines before coating process. In order to use suitable process regime and to define chemical structure and reaction type of intermediate temperature products, DTA-TG and FTIR analyses were performed in the film production using xerogels produced at different temperatures.Structural analysis of the films was performed using multipurpose XRD and surface morphology and topography was investigated using SEM/EDS. Surface chemistry of $K_2Ln_2Ti_3O_{10}$ (Ln= Nd, Gd, Sm, Dy) thin films was characterized in favour of X-ray photoelectron spectroscopy (XPS). Surface roughness analyses of samples were investigated with a surface profilometer. Mechanical properties of the films were investigated through nanoindenter. Optical Band Gap of thin films were measured by UV/VIS Spectrophotometer. Photocatalytical properties of thin films were characterized using sun test similator and ultraviolet-visible (UV-Vis) absorption spectra.

3.2 Materials

3.2.1 Substrate Materials

In the current research, Si(100) were used as substrate materials. All the substrates used were in high purity. The properties of the substrates were illustrated in Table 3.1

Table 3.1 Properties of substrate

Substrate	Surface	Crystal Structure	Preparation for coating process
Si	Polished	Cubic -Textured	Cutting with Logitech APD Annular& Peripheral Diamond Saw

Prior to deposition, Si(100) wafers were cleaned in an ultrasonic bath using 1:1 methanol-water or acetone media in order to eliminate impurities from the sample surface in as much as cleaning is a main issue in science and technology.

3.2.2 Chemical Materials

All types of precursors can be used, provided they are miscible. Metalic salts and alkoxides are the main precursor types. The general formula of a metallic salt is M_mX_n where M is the metal, X is an anionic group and m and n are stoichiometric coefficients. General formula for alkoxides is $M(OR)_n$, which indicates that they are a combination of a cation M with n alcohol groups ROH. For thin film production metal alkoxides are better than its salts as a precursor to achieve crack-free, pinholefree, homogeneous and textured films. In this study, alkoxide-based chemical materials which can be easily dissolved in solvents were used as precursor materials.

All chemical materials which were used for production of $K_2Ln_2Ti_3O_{10}$ (Ln= Nd, Gd, Sm, Dy) are listed in Table 3.2, indicating chemical types, names, formulas purity percentages and supplier.

3.2.3 Production Procedure

In this step there are four main solutions, these are Sm- KLTO, Dy- KLTO, Gd-KLTO and Nd-KLTO based solutions. According to the differences on the solutions, different solution stoichiometries were prepared. For KLTO based powder synthesis Lanthanum (III) 2, 4 pentanedionate hydrate and Potasssium 2, 4 Pentanedionate Hydrate were dissolved in propionic acid and glacial acetic acid (GAA) with a molar ratio 10:1. The solutions were rigorously and continuously stirred until completing dissolution of the precursors. Then, Titanium (IV) Isopropoxide (TTIP) and

Triethanolamine (TEA) were added to solution. At this stage, rare earth precursors such as, Sm^{+3}, Dy^{+3}, Gd^{+3} and Nd^{+3} based starting chemical materials were separately incorporated into this solution as dopant matters in order to prepare twelve different solutions. The names of solutions and amount of metal alkoxide (La, K, Ti, Dy, Nd,Sm and Gd) are given in Table 3.3. In this table, metal alkoxides are abbrivated like Me-p.

Table 3.2 All chemicals used for production of KLTO based thin film

Chemical Type	**Chemical**	**Formula**	**Purity**	**Supplier**
Precursors	Lanthanum (III) 2,4 Pentanedionate Hydrate	$C_{15}H_{21}\ LaO_6\ .xH_2O$	97.5%	Sigma Aldrich
	Potasssium 2,4 Pentanedionate Hydrate	$C_5H_7KO_2.xH_2O$	97%	Alfa Aesar
	Titanium (IV) Isopropoxide	$Ti(OCH(CH_3)_2)_4$	95%	Sigma Aldrich
Dopant Precursors	Dysprosium (III) 2,4 Pentanedionate Hydrate	$C_{15}H_{21}\ DyO_6\ .xH_2O$	99.9%	Alfa Aesar
	Neodymium (III) 2,4 Pentanedionate	$C_{15}H_{21}\ NdO_6$	99.9%	Alfa Aesar
	Samarium (III) Acetylacetonate Hydrate	$C_{15}H_{21}\ O_6Sm$	99.9%	Strem Chemicals
	Gadolinium (III) Acetylacetonate Hydrate	$C_{15}H_{21}\ GdO_6$	99.9%	Alfa Aesar
Solvent	Propionic Acid	$C_3H_6O_2$	-	-
Chelating Agent	Glacial Acetic Acid	$C_2H_4O_2$	-	T.Baker
Surfactant	Triethanolamine	$C_6H_{15}NO_3$	-	Merck

Final solutions were dried at 200 ^oC in air and then calcined 500 ^oC for 30 minutes with a heating rate of 5 ^oC/min and at 850 ^oC for 3 hours with a heating rate of 5^oC/min to produce Sm- KLTO, Dy- KLTO, Gd-KLTO and Nd-KLTO powders. After successfully synthesis of the powders, in order to obtain coating solutions,

powders were dispersed in propionic acid. The final concentration was adjusted to a concentration of 0.1 M.

Table 3.3 Solutions and amount of chemicals.

Solutions	La-p (g)	K-p (g)	Ti-p (ml)	Dy-p (g)	Nd-p (g)	Sm-p (g)	Gd-p (g)	P.acid (ml)	GAA (ml)	TEA (ml)
$K_2La_{1.9}Sm_{0.1}Ti_3O_{10}$	0.82	0.55	0.88	-	-	0.04	-	10	1	1
$K_2La_{1.5}Sm_{0.5}Ti_3O_{10}$	0.65	0.55	0.88	-	-	0.22	-	10	1	1
$K_2La_{1.1}Sm_{0.9}Ti_3O_{10}$	0.47	0.55	0.88	-	-	0.4	-	10	1	1
$K_2La_{1.9}Dy_{0.1}Ti_3O_{10}$	0.82	0.55	0.88	0.04	-	-	-	10	1	1
$K_2La_{1.5}Dy_{0.5}Ti_3O_{10}$	0.65	0.55	0.88	0.23	-	-	-	10	1	1
$K_2La_{1.1}Dy_{0.9}Ti_3O_{10}$	0.47	0.55	0.88	0.41	-	-	-	10	1	1
$K_2La_{1.9}Gd_{0.1}Ti_3O_{10}$	0.82	0.55	0.88	-	-	-	0.04	10	1	1
$K_2La_{1.5}Gd_{0.5}Ti_3O_{10}$	0.65	0.55	0.88	-	-	-	0.22	10	1	1
$K_2La_{1.1}Gd_{0.9}Ti_3O_{10}$	0.47	0.55	0.88	-	-	-	0.40	10	1	1
$K_2La_{1.9}Nd_{0.1}Ti_3O_{10}$	0.82	0.55	0.88	-	0.04	-	-	5	1	1
$K_2La_{1.5}Nd_{0.5}Ti_3O_{10}$	0.65	0.55	0.88	-	0.22	-	-	5	1	1
$K_2La_{1.1}Nd_{0.9}Ti_3O_{10}$	0.47	0.55	0.88	-	0.39	-	-	5	1	1

Final solutions were dried at 200 ^oC in air and then calcined 500 ^oC for 30 minutes with a heating rate of 5 ^oC/min and at 850 ^oC for 3 hours with a heating rate of 5^oC/min to produce Sm- KLTO, Dy- KLTO, Gd-KLTO and Nd-KLTO powders. After successfully synthesis of the powders, in order to obtain coating solutions, powders were dispersed in propionic acid. The final concentration was adjusted to a concentration of 0.1 M.

Film deposition on single crystal substrates was performed by spin coating technique. This is a compatible and precise technique for uniform deposition of metal oxide thin films, polymer coatings and metal organic thin films. A typical spin coating process involves deposition of a small drop (≈0.1-1 cc) of precursor solution onto the center of a substrate and then spinning the substrate at high speeds. Centripetal acceleration causes the excess amount of liquid to spread around leaving a thin film of precursor solution on the substrate surface. Schematically description

of this process is depicted in Figure 3.1 Final film thickness depends on the nature of the precursor solution as viscosity, drying rate and surface tension in addition to the parameters chosen for the spin coating process (Birlik, 2011).

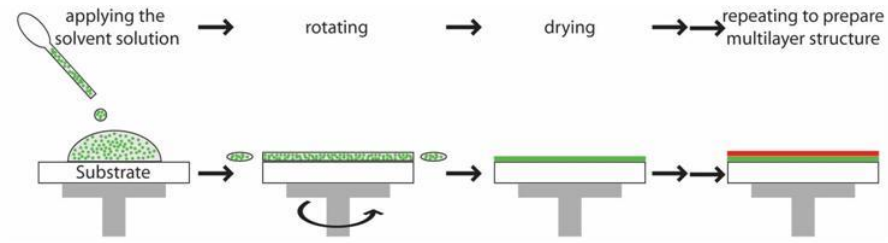

Figure 3.1 Spin coating process (Anonym, nd).

Spin 150 model spin coater was used to produce thin films on Si(100) substrates. The steps and rotation speed can be clearly seen in Table 3.4. As shown in the table spin coating process which is executed at air atmosphere possess four steps. To spread the solution and remove the excess of solution, at first and second 5 seconds the spinner accelerates up to 100 and 500 rpm, respectively. In the range of 10th sec. to 15th sec., spinner turns in a constant speed at 3000 rpm. At this step of operation, the deposited solution easily spreads on the substrate. Third step is the deceleration step here vaporizing of the volatiles and residual solutions were removed to improve surface quality and homogeneity in 10 seconds at 25 ^{o}C in air.

Table 3.4 The steps and rotation speed

Step	Time (s)	Rotation Speed (rpm)
1	5	100
2	10	500
3	15	3000
4	10	0

Finally, coated samples heat treated at 1000 ^{o}C for 5 hours with a heating rate of 5^{o}C/min under air and furnace cooled to room temperature . A flow chart for the thin film synthesis process is illustrated in Figure 3.2 .

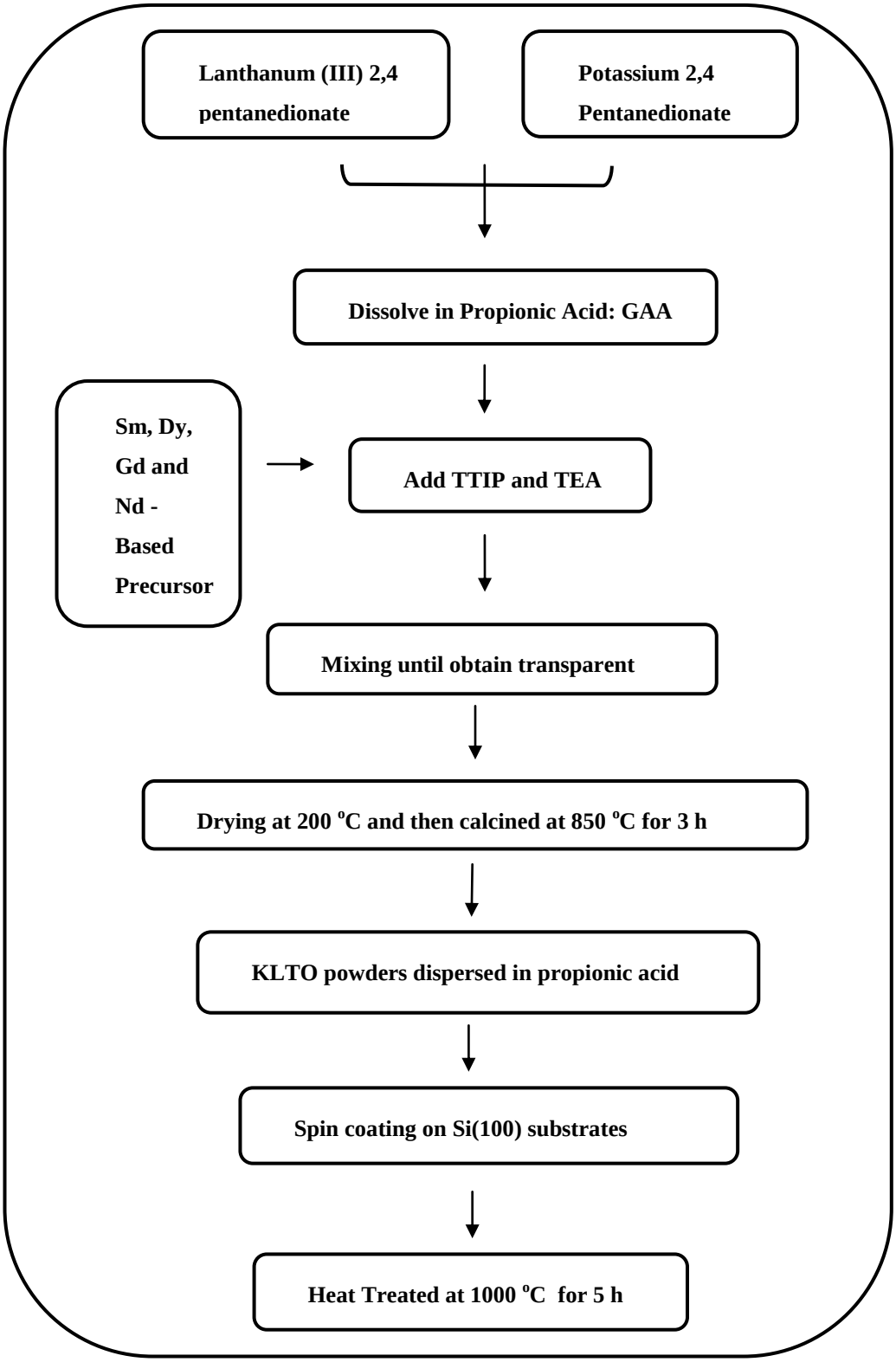

Figure 3.2 Flow chart for producing $K_2Ln_2Ti_3O_{10}$ (Ln= Nd, Gd, Sm, Dy) thin films

3.3 Characterization

3.3.1 Solution Characterization

In order to determine solution characteristics which affect thin film structure, pH values, turbidity, wettability and rheological properties of the prepared solutions were respectively measured by turbidimeter, pH meter, contact angle goniometer and rheometer machines before coating process.

3.3.1.1 pH Measurement

The pH measurement refers to determination of the activity of hydrogen ions in an aqueous solution. Many important properties of a solution can be determined from an accurate measurement of pH, including the acidity of a solution and the extent of a reaction in the solution. Many chemical processes and properties, such as the speed of a reaction and the solubility of a compound, can also depend greatly on the pH of a solution. In the study, pH values of the sol solutions were determined by standard pH meter with Mettler Tolede electrode.

3.3.1.2 Turbidity

Turbidity (or the relative cloudiness of a liquid) measurement gives the optical characteristics of suspended particles in a liquid. Light is passed through the sample and is scattered in all directions. The light that is scattered at a 90^{o} angle to the incident light is then detected by a photo diode and is converted into a signal linearized by the analyzer and displayed as an NTU (Nephelometric Turbidity Units) value. The more suspended particles there are in a liquid, the more light will be scattered, resulting in a higher NTU value. In the experiment, turbidity measurements of the prepared precursor solutions were performed by using VELB TB1model Turbidimeter. The sample was placed in the vessel with a dimension of Ø25 mm and height of 50 mm. Formazine is recognized throughout the world as a

primary standard. Formazine solution was used to calibrate the turbidity. It was determined whether powder based precursors are well-dissolved in the used solvent.

3.3.1.3 Contact Angle Measurement

The wetting behavior of the solutions on Si(100) substrates can be characterized by the contact angle γ, which is determined by the balance of the energies of the three interfaces: solid–liquid γ_{SL}, liquid–vapor γ_{LV} and solid–vapor γ_{SV}. The contact angle is given by Young‟s Equation 3.1, which is valid for the case of incomplete wetting:

$$\gamma_{SV} + \gamma_{SL} = \gamma_{LV} \cos\gamma \qquad (3.1)$$

In order to obtain a complete homogenous coverage of the Si(100) single crystal substrates leading to homogenous layer properties, a very small wetting angle close to 0^o was required.

Contact angle measurements of the solutions were performed with Contact Angle Meter-CAM 100 (KSV Instruments Ltd., Finland). It is a compact CCD camera based instrument for measurement of contact angles (CA) of liquids on solids. Goniometry involves the observation of a sessile drop of test liquid on a solid substrate. The basic elements of a goniometer include a light source, sample stage, lens and image capture. Contact angle can be accessed directly by measuring the angle formed between the solid and the tangent to the drop surface.

3.3.1.4 Rheological Measurements

The rheological measurements were conducted using a Bohlin Instruments CVO 100 Rheometer with 2^o conic plate geometry 60 mm in diameter and 0.7 μm gap sizes between plates. The viscosity values of KLTO solutions were performed at constant 300 Hertz frequency and 25 ^oC at single shear mode. The rheological properties of

the KLTO solutions were comparatively studied to characterize their gelation behaviors.

3.3.2 Material Characterization

3.3.2.1 Differential Thermal Analysis -Thermogravimetry (DTA- TG)

Thermal methods are based upon the measurement of the dynamic relationship between temperature and some property of the system such as mass and heat absorbed by or evolved from it. Differential Thermal Analysis (DTA) and Thermogravimetry (TG) are the most important thermal methods used in characterization of materials. In DTA the heat absorbed or emitted by a system is observed by measuring the temperature difference ΔT between the sample and an inert reference material (generally alumina powder), as the temperature of both is increased at a constant rate. TG analysis is concerned with the change in weight of a material as its temperatures changes. Many series of thermal analysis techniques can be combined with other non-thermal technique for valuable multiple-parameter information as in our DTA/TGA system. The decomposition of the gel was also studied under N_2 flowing by using Shimadzu DTG-60H Model Differential Thermal Analysis/ Thermal Gravimetric Analysis (DTA-TGA) in order to obtain information about the decomposition behavior of the gels to adjust the thermal treatment accordingly.

3.3.2.2 Fourier Transform Infrared Spectroscopy (FTIR)

FTIR is a common device for identifying types of chemical bonds in a molecule by producing an infrared absorption spectrum. By interpreting the infrared absorption spectrum, the chemical bonds in a molecule can be determined. In principle, molecular bonds vibrate at various frequencies depending on the elements and the type of bonds. For any given bond, there are several specific frequencies at which it can vibrate (Birlik, 2011).

FTIR spectrum of KLTO samples were recorded by using Perkin Elmer Spectrum BX model FTIR equipped with ATR apparatus to determine the chemical bonds and organic components in the samples. Samples were heat treated at 25 ^{o}C and 1000 ^{o}C before FTIR characterization. FTIR absorption spectra were measured over the range of 4000 to 400 cm^{-1}. According to the results, depending on temperature, variation of organic components concentration will be determined by Fluka library supplied by Perkin-Elmer.

3.3.2.3 X-ray Diffraction (XRD)

X-ray diffraction (XRD) is a technique which uses for identifying the crystalline phases presents in materials. XRD uses a beam of X-rays bombarding a specimen from various angles, θ. The X-rays are diffracted according to the as they are reflected from successive planes formed by the crystal lattice of the material. This diffraction can be expressed by Brag's Law of diffraction. By varying the angle of incidence, a diffraction pattern emerges that is characteristic of sample. The pattern is identified by comparing it with an internationally recognized data base Powder Diffraction File (PDF) reference patterns (Birlik, 2011).

XRD patterns of $K_2Ln_2Ti_3O_{10}$ (Ln= Nd, Gd, Sm, Dy) thin films were determined by Thermo- Scientific, ARL-K_α. Measurements were performed by applying 45 kV voltages and 44 mA current. The scanning speed was 2 ^{o}/min between 15^{o} and 80^{o}.

3.3.2.4 Scanning Electron Microscopy (SEM)

Scanning electron microscopy (SEM), is one of the most common analytical methods to examine surface morphology of the solid-state specimen. In SEM, a tiny high-energy electron beam is scanned across the sample surface. Series of radiations can be produced in terms of the interaction between the electron beam and the sample. Normally, two types of radiation are utilized for image formation: primary backscattered electrons and secondary electrons. Backscattered electrons reveal the compositional and topographical information of the specimen.

The secondary electron images produce a depth of field which shows the surface topography. The signal modulation of the two types of radiation is viewed as images in the CRT and provides the morphology, surface topology and composition of the specimen surface. The energy dispersive spectroscopy (EDS) is often attached to the SEM. The X-rays generated from the interaction between the electron beam and the specimen is used to identify and measure quantitatively the elemental composition of the specimen. Therefore, SEM/EDS can detect the elemental composition and obtain the morphology of the specimen simultaneously. (Ebeoglugil, 2011) In this study, the surface and elemental composition of the $K_2Ln_2Ti_3O_{10}$ (Ln= Nd, Gd, Sm, Dy) thin films were examined by using JEOL JSM-6060 instrument operating at an accelerating voltage of 15 kV.

3.3.2.5 X-ray Photoelectron Spectroscopy (XPS)

X-ray photoelectron spectroscopy (XPS) is an analyze technique which provides both elemental and chemical state information about sample material. XPS spectra are obtained by irradiating a material with a beam of X-rays while simultaneously measuring the kinetic energy and number of electrons that escape from the top 1 to 10 nm of the material being analyzed. XPS requires ultra-high vacuum (UHV) conditions and detects all elements with an atomic number (Z) of 3 (lithium) and above (Crist, 2014). In this study, elemental analyses of $K_2Ln_2Ti_3O_{10}$ (Ln= Nd, Gd, Sm, Dy) were analyzed via XPS (Thermo-Scientific Al-K_α) especially to determine substituting elements in films.

3.3.2.6 Surface Roughness

Profilometer is a measuring instrument used to measure a surface profile of the films, in order to quantify its roughness and thickness. While the historical notion of a profilometer was a device similar to a phonograph that measures a surface as the surface is moved relative to the contact profilometer's stylus, this notion is changing with the emergence of numerous non-contact profilometery techniques. The

roughness of the films was determined through Ambios Technology XP-2 Surface Profilometer.

3.3.2.7 Mechanical Tests

Hardness is defined as the characteristic ability of a material to resist penetration or abrasion by other bodies. Indentation testing is a simple method that consists essentially of touching the material of interest whose mechanical properties such as elastic modulus and hardness.

Nanoindentation measurements were performed using a nanoindentation system (IBIS, Fischer-Cripps Laboratories, Australia). We have used a three-side pyramid (Berkovich) diamond indenter. The area function, which is used to calculate contact area A_c from contact depth hc, was carefully calibrated by using a fused silica sample, prior to the experiments. Samples were sticked on a low contraction resin and cut in 2 x 2 cm. Load of 5 mN were used for the tests.

Adhesion strength of coatings were evaluated by using a scanning scratch tester (IBIS, Fischer-Cripps Laboratories, Australia) with a 15 μm tip radius diamond stylus. During the test, a stylus was drawn on coating surface with a sliding speed of 5 $\mu m.s^{-1}$ keeping scanning amplitude of 10 μm which perpendicular to the scratching direction at the same time. Load was carried out progressively to the stylus with a loading speed of 2 $\mu m.s^{-1}$. As a result of test, critical force is defined as adhesion strength.

3.3.2.8 Optical Band Gap

In the case of a thin film on the surface of a glass, both the top and bottom surfaces of the film reflect light, with the total amount reflected being dependent upon the sum of these two reflections. Furthermore, these two reflections may add together constructively or destructively depending upon their phase relationship. This phenomenon is due to the wavelike nature of light, with the phase relationship

determined by the difference in optical path lengths of the two reflections. The resulting interference pattern can be used to determine the thickness of the film according to the formula;

$$d = \frac{m}{2D_n\sqrt{n^2-(sin\emptyset)^2}} \quad (3.2)$$

where; d=film thickness, m=number of patterns in wavenumber region used, n=refractive index, θ=angle of incident (measured by spectrophotometer during measurement), D_n= wave number region used (Erol, 2009). Optical Band Gap of thin films were measured at selected wavelengths using V-530 JASCO UV/VIS Spectrophotometer.

3.3.2.9 Photocatalytic Activity Test

The photocatalytic degradation processes were realized to treat methylene blue . Photocatalytic degradation experiments were carried out in a solar box ATLAS SUNTEST CPS+ which is simulating natural radiation. The light source has a vapor xenon lamp (300 nm < λ <800 nm) and the power can change between 250 and 765 W/m^2 that showned in the Figure 3.3.

Methylene blue (MB) is a type of thiazine dye and azo dye. and it has large scale utilization in industries. The chemical compound of Methylene Blue is a type of heterocyclic aromatic and its chemical formula is formed as $C_{16}H_{18}ClN_3S.\ 3H_2O$ (3,7-bis(dimethylamino)-fenazotionium chloride). The areas of usage are coloring the papers, hair dye, fabric dying and wool dying. The applications of methylene blue are mostly from textile industries. It is commonly used in dyestuff applications and as a redox indicator. For this reason, it is the major pollutant of textile industry wastewaters (Yao & Wang, 2010).

Figure 3.3 Sun Test CPS +

When the methylene blue dissolves in water, three absorbances can be seen in the UV - visible beam zone. The first absorbance band is 264 nm, and the two others are 291 nm and 664 nm, respectively. The absorbance 291 nm and 664 nm are mostly used for removing the methylene blue. Within the experiments, 664 nm wavelengths is chosen to make the analysis in visible radiation (Yao & Wang, 2010). The absorbance of the degradation experiments were measured by using Shimadzu UVmini-1240 spectrophotometer.

CHAPTER FOUR
RESULTS AND DISCUSSION

4.1 Solution Characterization

4.1.1 pH

The pH value is a measure of the activity of hydrogen ions (H^+) in a solution therefore, its acidity. Solutions with pH values lower than 7 exhibit acidic properties, while pH values higher than 7 are considered as basic. pH value is an important parameter in the solution deposition processes because it directly affects the hydrolyses, condensation and complexation reactions.

Determination of solution characteristics is a key factor in sol-gel processing or solution based deposition. Since pH value of the solution is an important factor influencing the formation of the polymeric three-dimensional structure of the gel during the gelation process, it should be taken into consideration while preparing solutions. While ramified structure is randomly formed in acidic conditions, separated clusters are formed from the solutions showing basic characters (Pierre, 1998).

Due to these factors influencing solution characteristics and thus film morphology, pH value should be measured after preparation of solutions. pH values of KLTO based solutions were illustrated in Table 4.1. It is clear that solutions exhibit acidic characters. Because alkoxide based precursors were used to prepare the solutions, the values of pH were determined in the range of 3.08- 4.42 which are not very low .If we have used salt based precursors these values would be decreased to 1. This is the general characteristic of the salt based precursors thanks to Cl^-, NO_2^-, SO_2^-. The another reeason must be propionic acid and glacial acetic acid (GAA) which were used to dissolve precursor powders.

Table 4.1 pH values of KLTO based solutions

Samples	pH
$K_2La_{1.9}Sm_{0.1}Ti_3O_{10}$	4.42
$K_2La_{1.5}Sm_{0.5}Ti_3O_{10}$	4.39
$K_2La_{1.1}Sm_{0.9}Ti_3O_{10}$	4.41
$K_2La_{1.9}Dy_{0.1}Ti_3O_{10}$	3.24
$K_2La_{1.5}Dy_{0.5}Ti_3O_{10}$	3.23
$K_2La_{1.1}Dy_{0.9}Ti_3O_{10}$	3.21
$K_2La_{1.9}Gd_{0.1}Ti_3O_{10}$	3.12
$K_2La_{1.5}Gd_{0.5}Ti_3O_{10}$	3.08
$K_2La_{1.1}Gd_{0.9}Ti_3O_{10}$	3.09
$K_2La_{1.9}Nd_{0.1}Ti_3O_{10}$	3.91
$K_2La_{1.5}Nd_{0.5}Ti_3O_{10}$	3.92
$K_2La_{1.1}Nd_{0.9}Ti_3O_{10}$	3.93

4.1.2 Turbidity

Turbidity (or the relative cloudiness of a liquid) measurement gives the optical characteristics of suspended particles in a liquid (Wilde & Gibs, n.d.). With this experiments, whether powder precursor materials are dissolved very well in solutions is understood by looking ntu values before coating process. As mentioned before, the turbidity values of the solutions vary in the range of 0 ntu and 1000 ntu. It is interpreted that powder based precursors are completely dissolved as turbidity value approaches to 0 ntu and they are not dissolved and some powder particles are suspended in a solution as it appoaches to 1000 ntu. The fabrication of $K_2Ln_2Ti_3O_{10}$ (Ln= Nd, Gd, Sm, Dy) powder or thin films is directly related to turbidity values of the solutions, which is 0 ntu. Turbidity values of the KLTO based solutions were illustrated in Table 4.2. The values of the dissolved solutions were found in the range of 15.72-35.23 ntu , which are reasonable for thin film production. Based on the these values, it can be pointed that powder based precursors are completely dissolved in the solutions. Moreover, these values present an important clue for further processing. It is worth noticing that optimum structural, thermal, microstructural, mechanical, properties are not obtained using undissolved solutions.

Table 4.2 Turbidity value of the KLTO based solutions

Samples	Turbidity (ntu)
$K_2La_{1.9}Sm_{0.1}Ti_3O_{10}$	15.72
$K_2La_{1.5}Sm_{0.5}Ti_3O_{10}$	17.28
$K_2La_{1.1}Sm_{0.9}Ti_3O_{10}$	16.24
$K_2La_{1.9}Dy_{0.1}Ti_3O_{10}$	19.2
$K_2La_{1.5}Dy_{0.5}Ti_3O_{10}$	18.63
$K_2La_{1.1}Dy_{0.9}Ti_3O_{10}$	21.45
$K_2La_{1.9}Gd_{0.1}Ti_3O_{10}$	21.2
$K_2La_{1.5}Gd_{0.5}Ti_3O_{10}$	19.83
$K_2La_{1.1}Gd_{0.9}Ti_3O_{10}$	17.31
$K_2La_{1.9}Nd_{0.1}Ti_3O_{10}$	17.76
$K_2La_{1.5}Nd_{0.5}Ti_3O_{10}$	28.52
$K_2La_{1.1}Nd_{0.9}Ti_3O_{10}$	35.23

4.1.3 Wettability Behaviors

Contact angle values of each solution were measured with contact angle goniometer. All measurements were performed on Si substrates. It is noticed that all contact angle values are changing from 3^0 to 4^0. Generally speaking, since the contact angles of the solutions approaches to 0^0, these results are reasonable before coating process and thus the solutions can easily wet Si substrate. Due to these reasons , very thin and continous films can be deposited on Si substrate.

4.1.4 Rheological Properties

Rheological behaviour can be an important property to characterize sols and sol-gel transition. With this context, the viscosity $K_2Ln_2Ti_3O_{10}$ (Ln= Nd, Gd, Sm, Dy) solution was measured as a function of time.

Viscosity is an internal property of a fluid that offers resistance to flow. In other words, it is a measure of the resistance of a fluid to deform under shear stress. Viscosity describes a fluid's internal resistance to flow and may be thought of as a

measure of fluid friction. Figures 4.1 - 4.4 shows the viscosity behavior of the solutions.

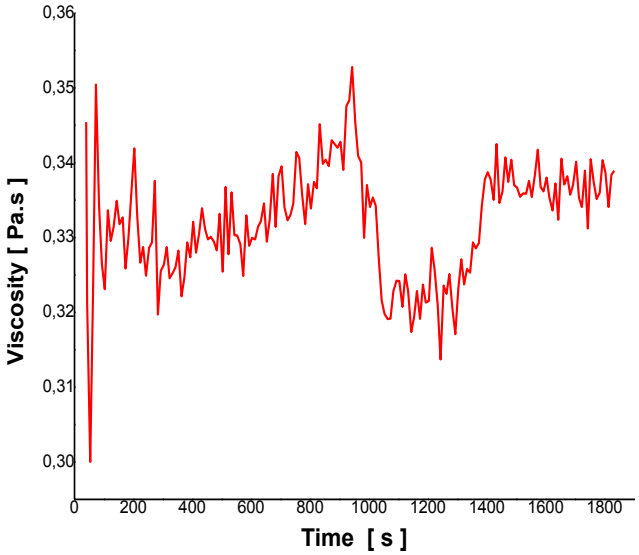

Figure 4.1 Viscosity values of Gd-KLTO solution

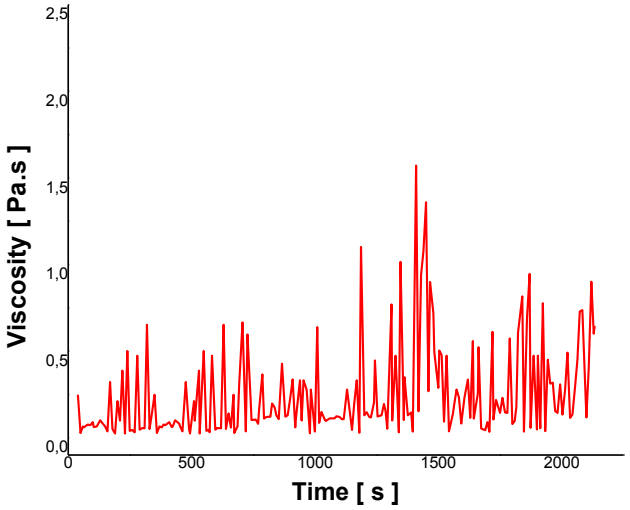

Figure 4.2 Viscosity values of Sm-KLTO solution

Gelation occurs when aggregation of particles or molecules takes place in a liquid, under the action of Van der Walls forces or via the formation of covalent or

noncovalent bonds. The process can be investigated using rheological measurement techniques (Ebeoglugil, 2011).

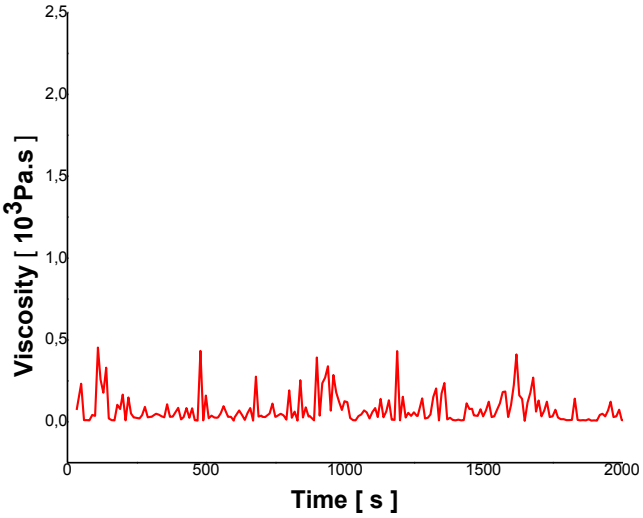

Figure 4.3 Viscosity values of Dy-KLTO solution

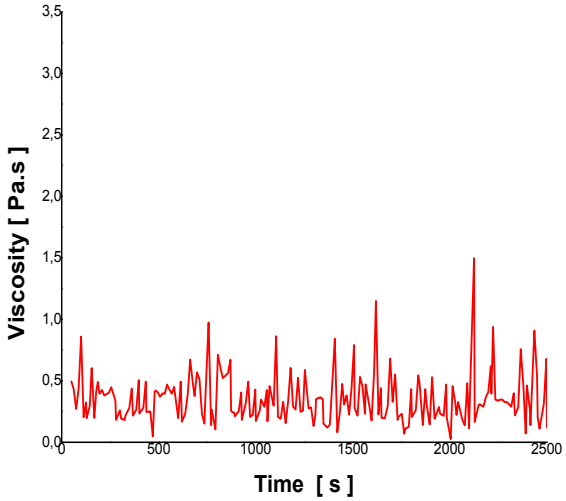

Figure 4.4 Viscosity values of Nd-KLTO solution

Depending on Figures 4.1 - 4.4, it can be understood that the average viscosity value of the $K_2Ln_2Ti_3O_{10}$ (Ln= Nd, Gd, Sm, Dy) solutions were found to be 0.3 Pa.s. These low viscosity values are advantageous for thin film production in collaboration with low contact angle value. It should be kept in mind that higher viscosity values can lead to form thicker films with microcracks.

For Gd-KLTO solution, at first viscosity value decreases with increasing temperature due to evaporation of solvent in the solutions, but then they reach a constant value. Peaks of Sm-KLTO solutions may be resulted of noises of the device. The viscosity value of the Nd-KLTO and Dy-KLTO solutions is more stable than Sm-KLTO and Gd - KLTO.

4.2 Material Characterization

4.2.1 DTA/TG Analyses

Simultaneous thermal analysis (DTA-TG, SHIMADZU) measurements were carried out in oxygen atmosphere from room temperature to 1000 ^{o}C at heating rate of 10 ^{o}C /min. Prior to measurements, $K_2Ln_2Ti_3O_{10}$ (Ln= Nd, Gd, Sm, Dy) xerogel powders were firstly dried at room temperature and subsequently fired to in the gel structure at 300 ^{o}C for 30 minutes in air.

It is important to appreciate the process optimization mechanism leading to thermal behavior of KLTO based powder xerogel to obtain regular heat treatment regime from room temperature to phase formation temperature.

Figures 4.5, 4.6, 4.7 and 4.8 depicts DTA-TGA curves of the thermal behavior of such a sample resembles that of other ones. The several temperatures are critical for formation of KLTO phase and heat treatment regime. Thus these critical temperatures and also three thermal phenomena were determined from the curves for each xerogel. One of them was the solvent removal which started at temperature of approximately 200 ^{o}C and reached the strongest peaks at 300 ^{o}C. At this range, the endothermic reaction is mostly due to evaporation of volatile organic components. The second phenomena was the combustion of OR groups coming from Nd, Gd, Sm, Dy based precursor, solvent, and chelating agent in the samples between 400 and 600 ^{o}C.

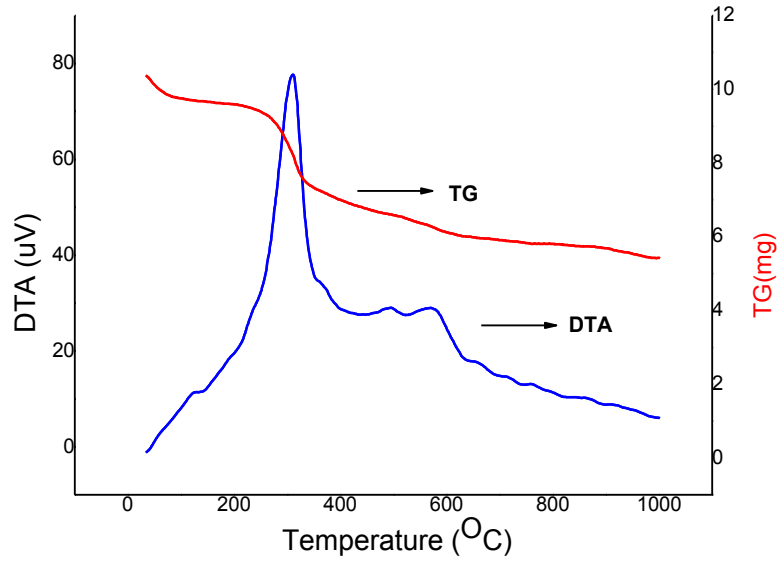

Figure 4.5 DTA/TG curve of Gd-KLTO dried at 300 ^{O}C for 30 min in air

Generally speaking, the last stage should have been the formation of ceramic oxides after 600 ^{o}C. Nevertheless, we could not determine oxidation peaks with high intensity in the range of these temperatures.

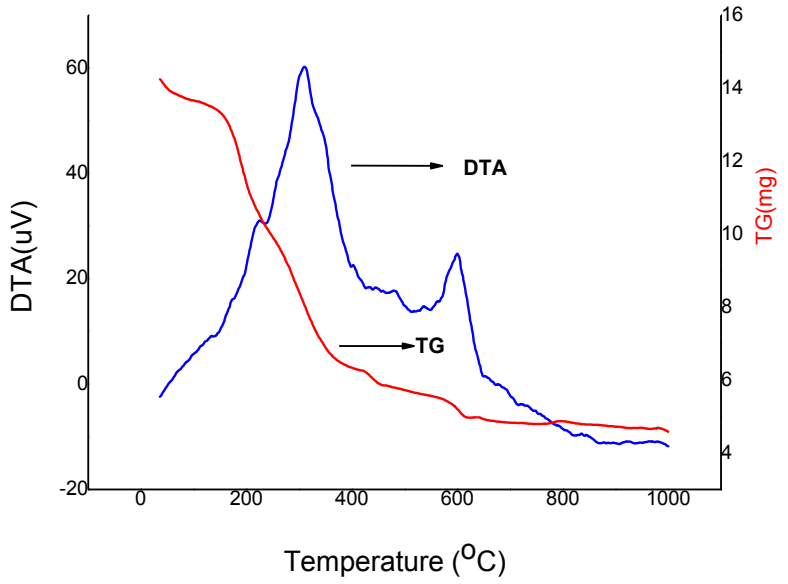

Figure 4.6 DTA/TG curve of Sm-KLTO dried at 300 ^{O}C for 30 min in air

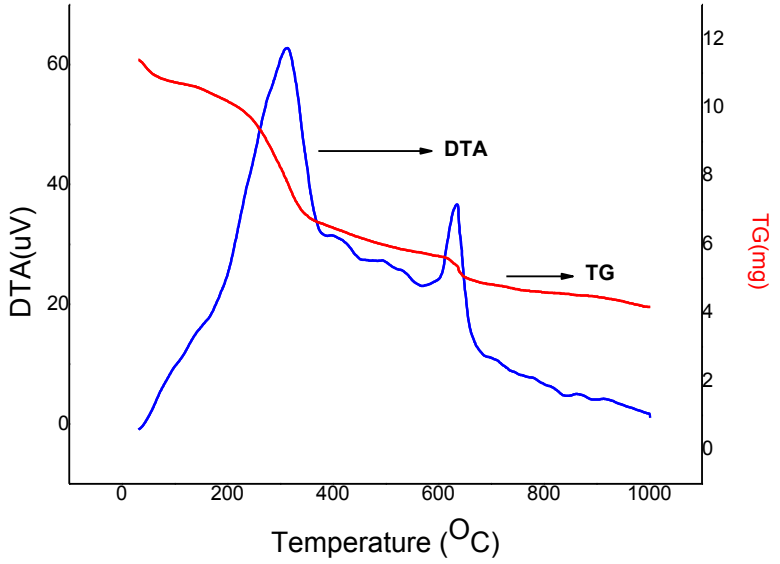

Figure 4.7 DTA/TG curve of Dy-KLTO l dried at 300 ^{O}C for 30 min in air

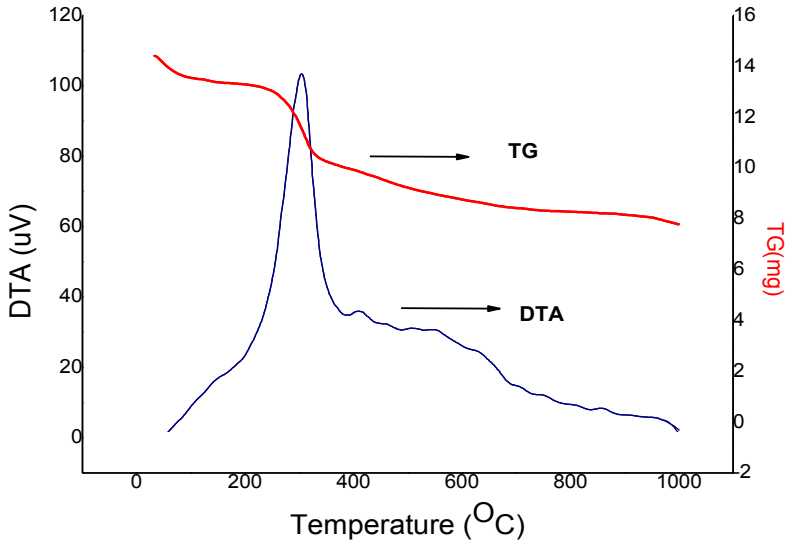

Figure 4.8 DTA/TG curve of Nd-KLTO dried at 300 ^{O}C for 30 min in air

By using DTA/TG weight loss versus time with increasing temperature is determined too. TG analysis of the xerogels are important since this experiment gives information about the final film weight. With this information one can decide or get opinion about the film density, morphology. It can be seen from TG curves that total weight loss were determined as 40 % , 64%, 63%, 46% from room temperature to

1000 ^{O}C for Gd-KLTO, Sm-KLTO, Dy-KLTO and Nd-KLTO, respectively. Acoording to weight loss of the Gd-KLTO xerogel is denser than that of the others. Thus it has the minimum weight loss. With this respect weight losses of Nd-KLTO, Sm-KLTO and Dy-KLTO xerogels are higher than that of Gd-KLTO xerogel. It can be thought that the nature of Gd-KLTO xerogel caused this low weight loss.

4.2.2 FTIR Analyses

The aim of this section is to elucidate what type bonding can occur during heat treatment of KLTO based materials, to understand the nature of their bonds, and thus to assist to be determined their process optimization. The resulting spectra produce a profile of the sample, a distinctive molecular fingerprint that can be used to easily screen and scan samples from many different components. It is an effective analytical instrument for detecting functional groups and characterizing covalent bonding information (Kayatekin, 2006).

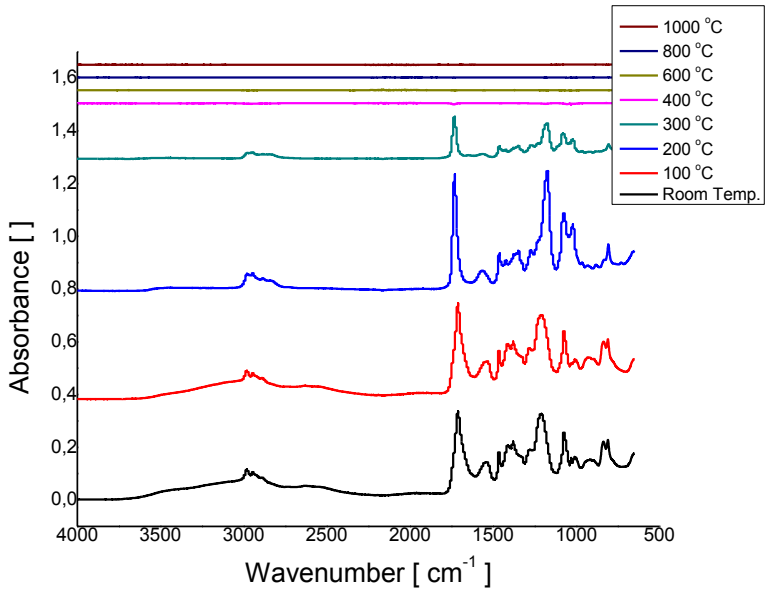

Figure 4.9 FTIR spectra of Sm-KLTO heat treated at different temperaturres

For that reason, FTIR spectrum of xerogels from room temperature to 1000 ^{o}C were recorded with FTIR spectrophotometer (Perkin Elmer). The spectra were represented as relative absorbance versus the wave number (cm^{-1}). Figures 4.9, 4.10, 4.11 and 4.12 involve FTIR absorbance spectra of Sm, Dy, Gd and Nd based

xerogels heat treated at different temperatures in air. It is clear from the figures that all of xerogels showed the nearly similar spectra and there are two strong bands observed for all samples.

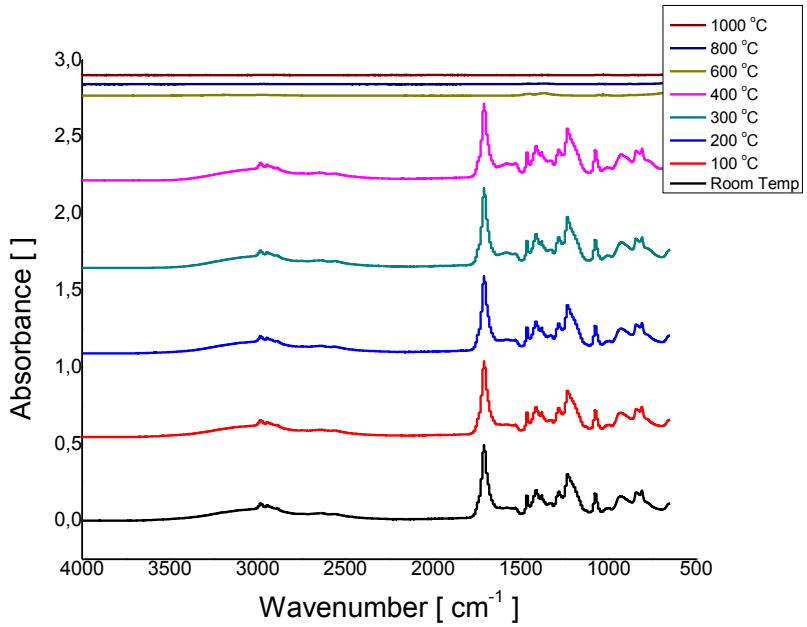

Figure 4.10 FTIR spectra of Gd -KLTO heat treated at different temperaturres

The peak, which occurred near 3000 cm^{-1} is assigned to the C-H (Besergil, 2015). This peak resulted from different starting precursors, chelating agent and solvents.

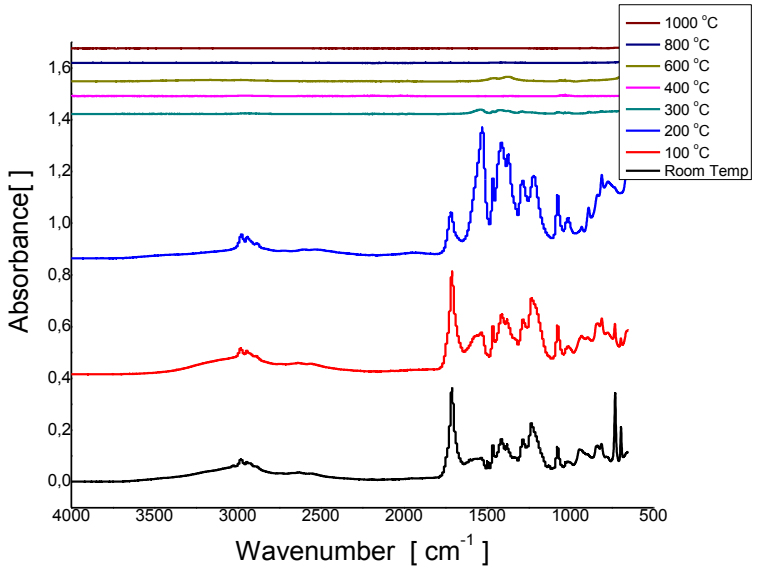

Figure 4.11 FTIR spectra of Nd -KLTO heat treated at different temperaturres

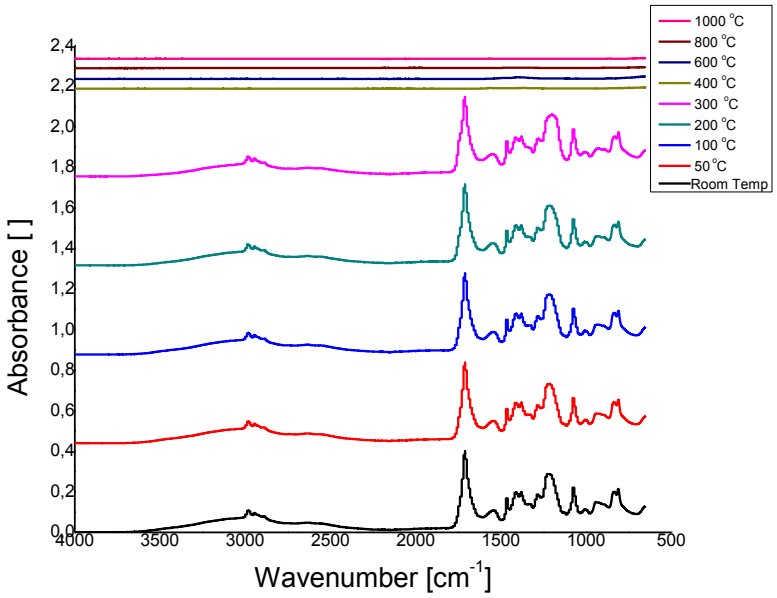

Figure 4.12 FTIR spectra of Dy -KLTO heat treated at different temperaturres

Bands at 1750-750 cm^{-1} belong to -OH, -CH_2-, and M-OCOO-M. Upon increasing heat treatment temperature from 25 ^oC to 400 ^oC, the frequencies of -OH, -CH_2-, and M-OCOO-M bands decreased. This means that the organic content and hydroxyl were removed as a function of heat treatment temperatures. Chen et al. (2005), stated that the signal which is in the range of 400-1200 cm-1 shows the characteristics formationof O-Ti-O.

4.2.3 XRD Analyses

X-ray diffraction (XRD) is a technique which uses for identifying the crystalline phases presents in materials. XRD uses a beam of X-rays bombarding a specimen from various angles, θ.

XRD patterns of $K_2Ln_2Ti_3O_{10}$ (Ln= Nd, Gd, Sm, Dy) thin films were represented in Figures 4.13-4.24. The obtained patterns were compared device library with search match operation. After deposition of the KLTO based solution to the Si(100) substrate and heat treatments, the pattern was obtained. As shown in that pattern KLTO phase was obtained in this films with low intensities because of very thin film thickness.

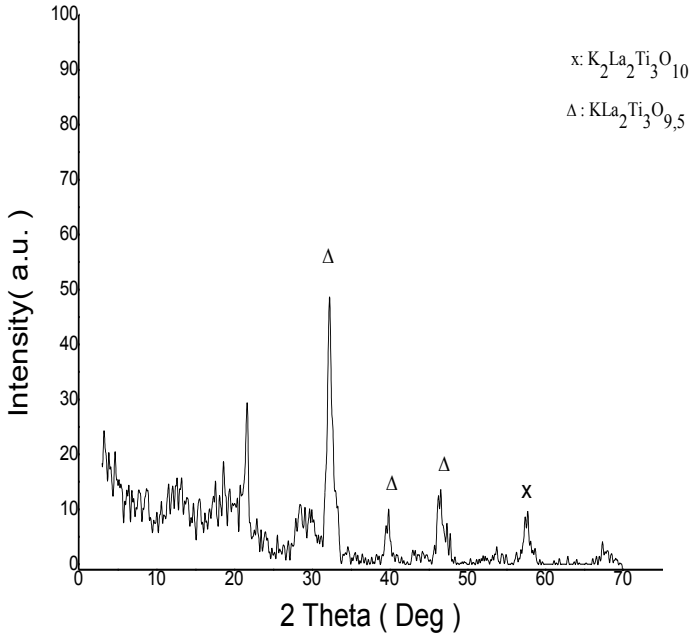

Figure 4.13 XRD pattern of $K_2La_{1.9}Sm_{0.1}Ti_3O_{10}$ thin film on Si substrate

This is evidence from figures that the intensity of peaks isn't affected when increasing dopant percentages; but XRD patterns of doped KLTO thin films depending on different type of dopants.

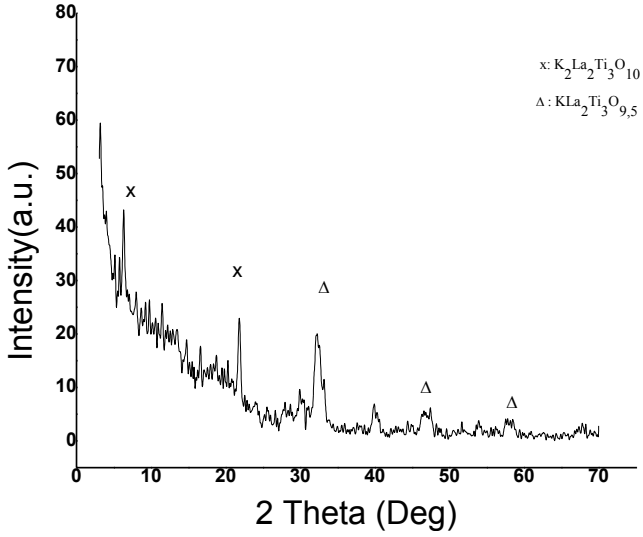

Figure 4.14 XRD pattern of $K_2La_{1.5}Sm_{0.5}Ti_3O_{10}$ thin film on Si substrate

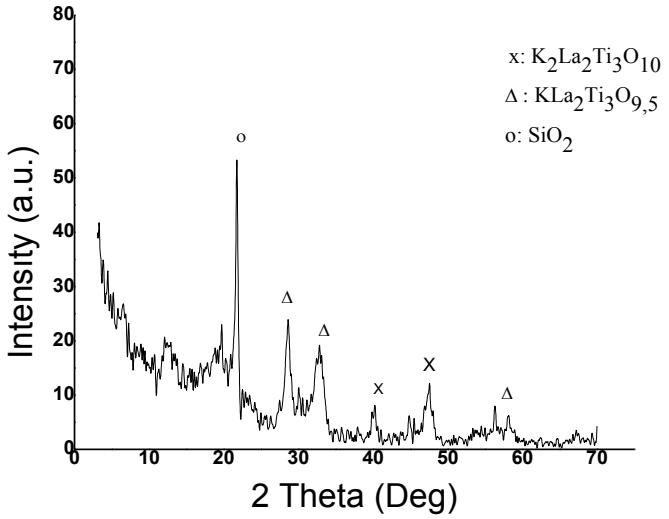

Figure 4.15 XRD pattern of $K_2La_{1.1}Sm_{0.9}Ti_3O_{10}$ thin film on Si substrate

$KLa_2Ti_3O_{9.5}$ phases was observed in the patterns. This must be resulted from time or temperature of heat treatment. Since there is not enough time for diffusion ions could not take their place in the structure. Another alternative reason might be that; while weighting precursors some mistakes may be done and these make stoichimetry to be broken. These kinds of unwanted phases may affect the structure of films.

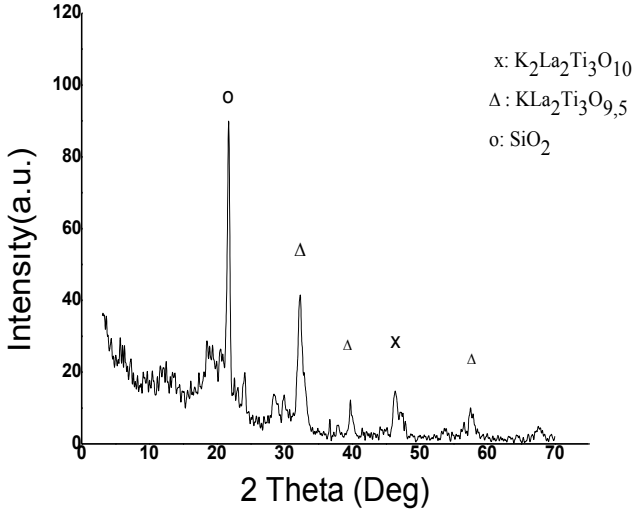

Figure 4.16 XRD pattern of $K_2La_{1.9}Dy_{0.1}Ti_3O_{10}$ thin film on Si substrate

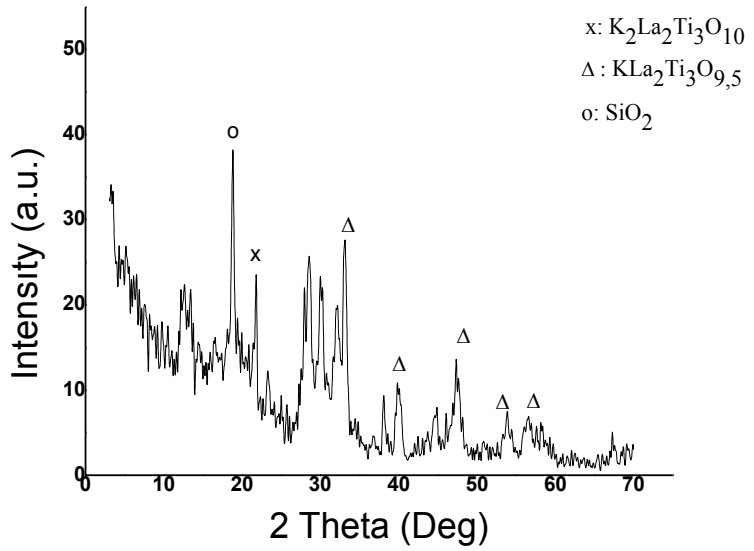

Figure 4.17 XRD pattern of $K_2La_{1.5}Dy_{0.5}Ti_3O_{10}$ thin film on Si substrate

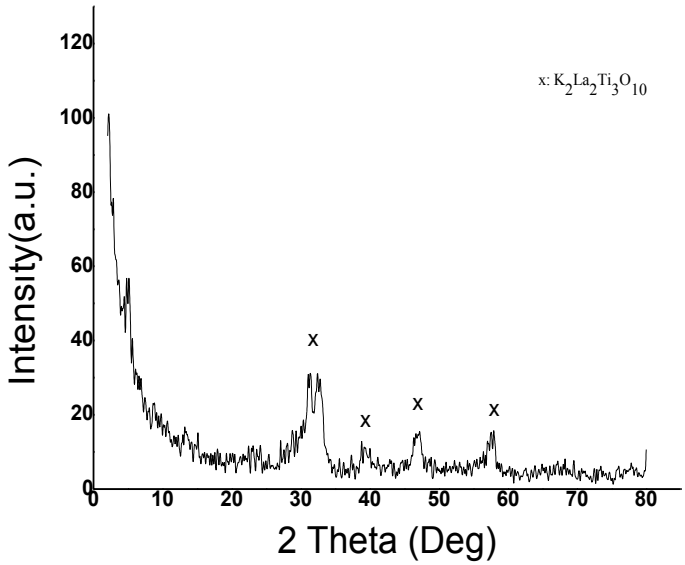

Figure 4.18 XRD pattern of $K_2La_{1.1}Dy_{0.9}Ti_3O_{10}$ thin film on Si substrate

It can be also seen SiO_2 phases in the patterns. This must be resulted from oxidation of Si(100) substrate during heat treatment.

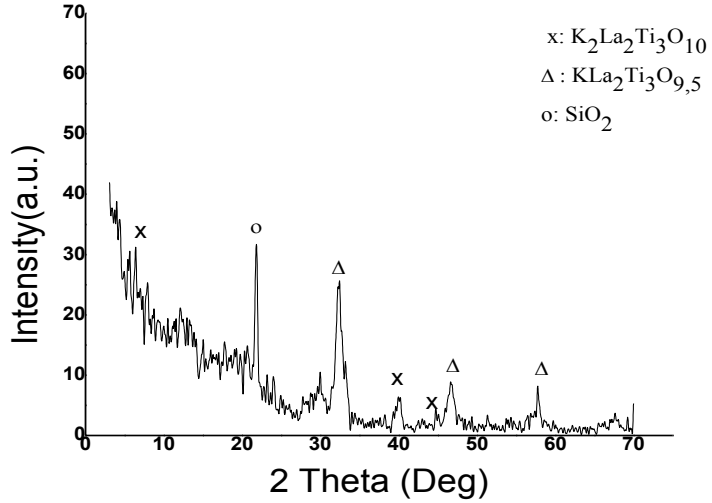

Figure 4.19 XRD pattern of $K_2La_{1.9}Gd_{0.1}Ti_3O_{10}$ thin film on Si substrate

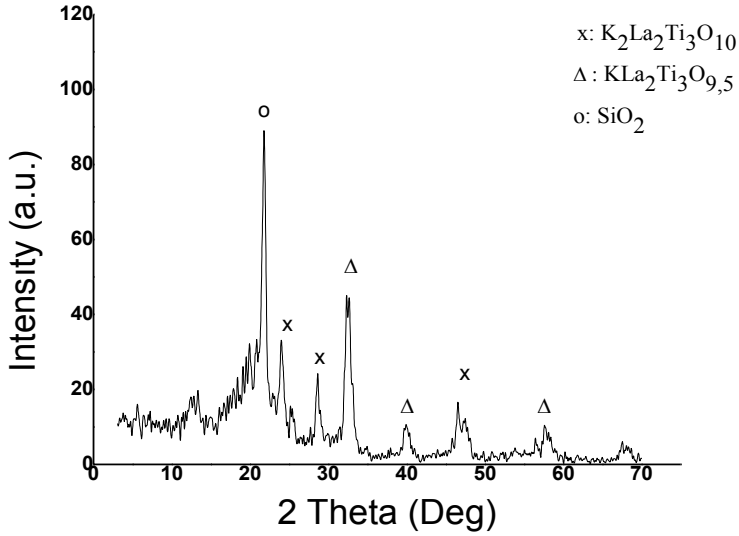

Figure 4.20 XRD pattern of $K_2La_{1.5}Gd_{0.5}Ti_3O_{10}$ thin film on Si substrate

In the XRD patterns of Sm, Dy, Nd, Gd doped KLTO thin films; $K_2La_2Ti_3O_{10}$ phase was obtained. Because of different stoichimetry and dopants , the location of peaks differ. However, when the diffraction peaks compared to the literature, it showed that crystalline $K_2La_2Ti_3O_{10}$ was obtained (Cui et al., 2013).

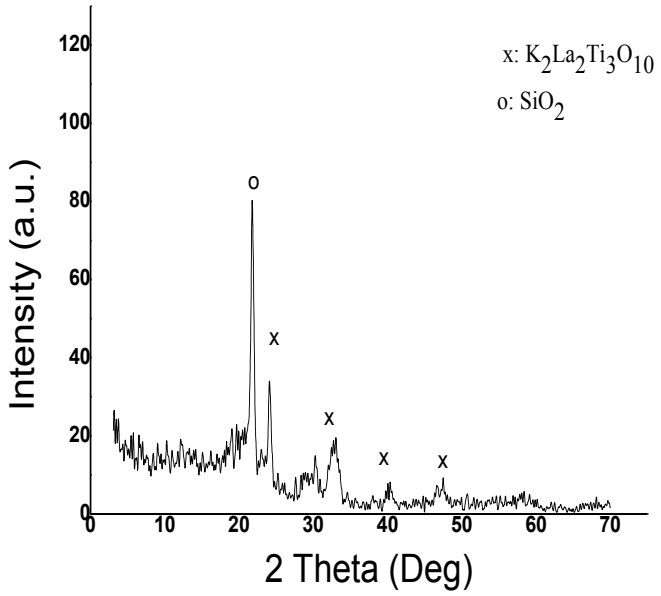

Figure 4.21 XRD pattern of $K_2La_{1.1}Gd_{0.9}Ti_3O_{10}$ thin film on Si substrate

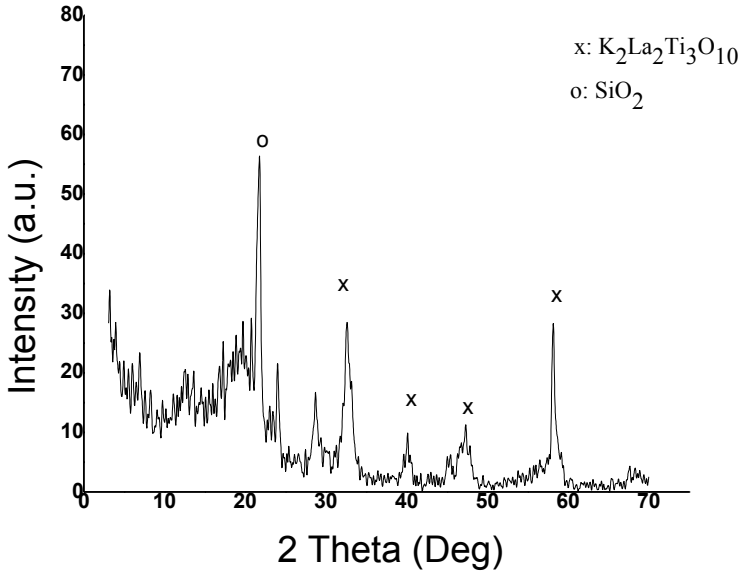

Figure 4.22 XRD pattern of $K_2La_{1.9}Nd_{0.1}Ti_3O_{10}$ thin film on Si substrate

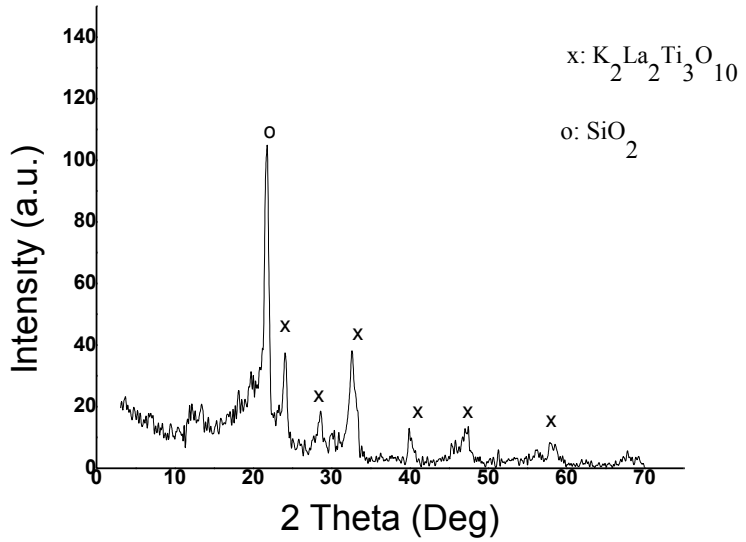

Figure 4.23 XRD pattern of $K_2La_{1.5}Nd_{0.5}Ti_3O_{10}$ thin film on Si substrate

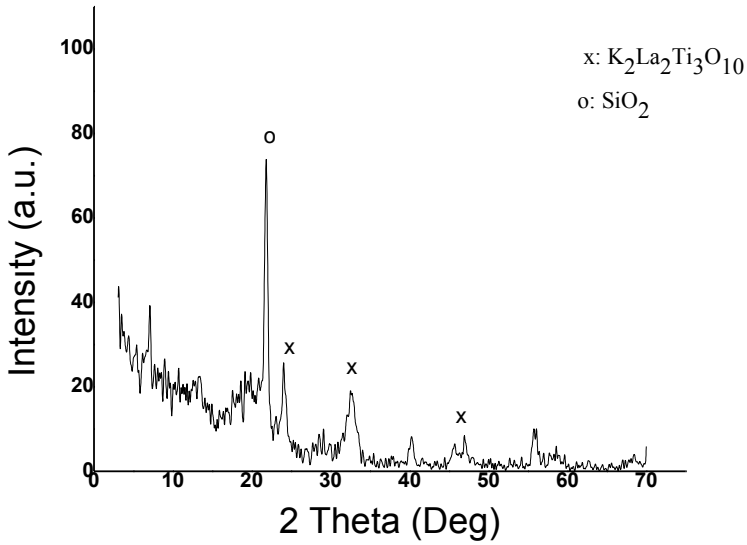

Figure 4.24 XRD pattern of $K_2La_{1.1}Nd_{0.9}Ti_3O_{10}$ thin film on Si substrate

4.2.4 Microstructural Analyses

In order to examine the surface properties of $K_2Ln_2Ti_3O_{10}$ (Ln= Nd, Gd, Sm, Dy) thin films and control whether KLTO powder homogenously disperse in propionic

acid, SEM micrographs at different magnifications were taken and shown in Figure 4.25- 4.36. The morphology of the films is an important parameter that affects photocatalytical properties. Morphology of the films are directly affected from the processing parameters such as; solution concentration, pH, viscosity, film thickness, coating technique, and heat treatment regime.

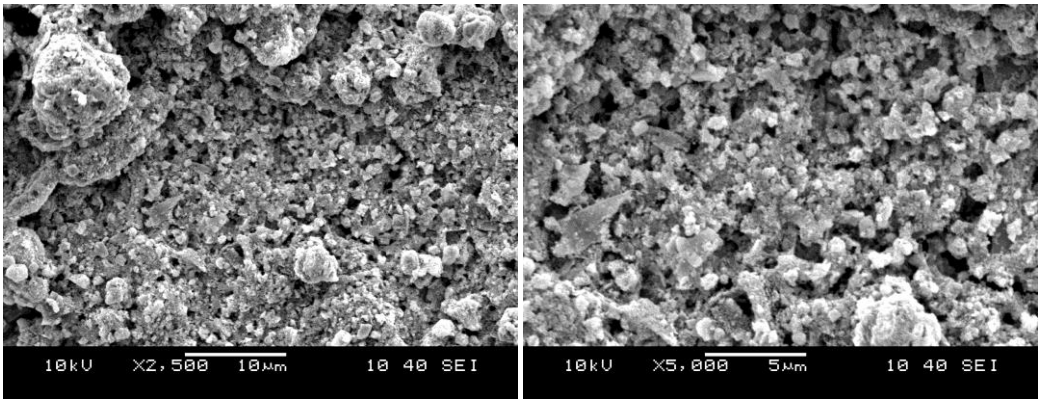

Figure 4.25 SEM images of $K_2La_{1.9}Sm_{0.1}Ti_3O_{10}$ thin film

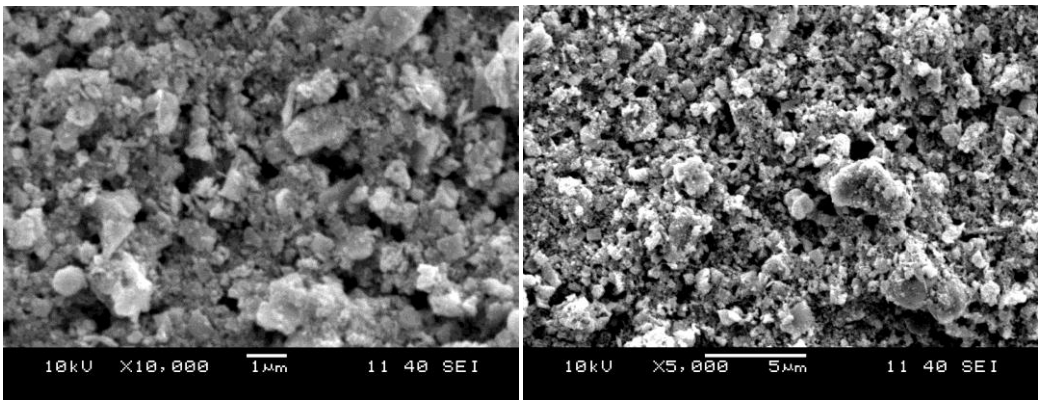

Figure 4.26 SEM images of $K_2La_{1.5}Sm_{0.5}Ti_3O_{10}$ thin film

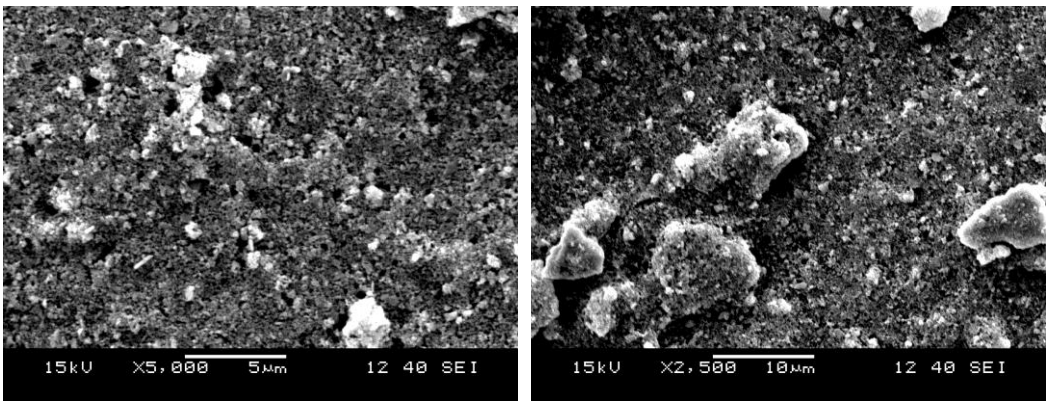

Figure 4.27 SEM images of $K_2La_{1.1}Sm_{0.9}Ti_3O_{10}$ thin film

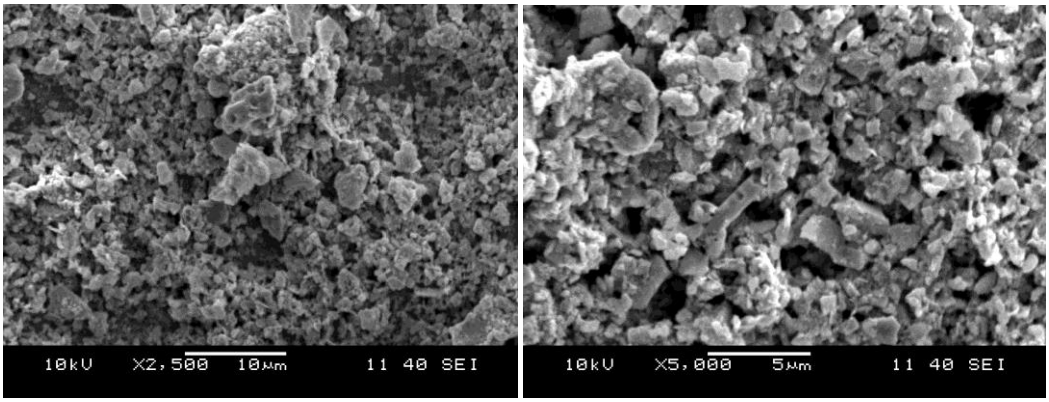

Figure 4.28 SEM images of $K_2La_{1.9}Dy_{0.1}Ti_3O_{10}$ thin film

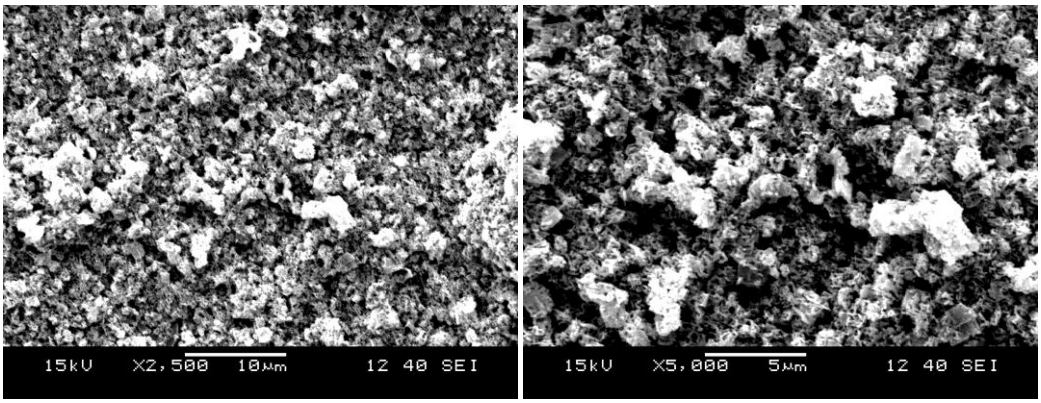

Figure 4.29 SEM images of $K_2La_{1.5}Dy_{0.5}Ti_3O_{10}$ thin film

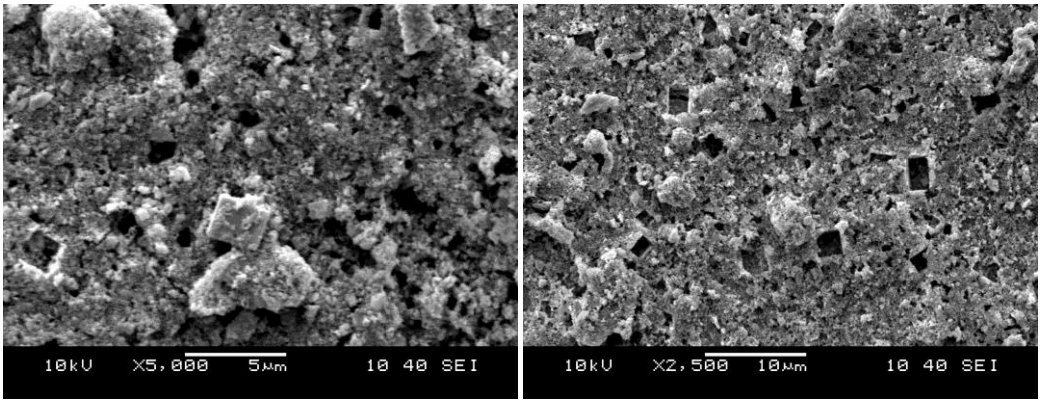

Figure 4.30 SEM images of $K_2La_{1.1}Dy_{0.9}Ti_3O_{10}$ thin film

The SEM micrograph shows that there are inhomogeneous on the surface. The surface morphology occurred because of coating process and thermal treatment effects of our production steps. Agglomerated particles and different shaped structures are seen. Nevertheless, it was found that the surface morphologies of films are consistent with literature (Lee, 2003).

As mentioned in the literature, surface area is crucial parameter for photocatalytical application and the surface area that acting with pollution is increased, the photocatalytic efficiency is also rised (Bakuy, 2009).

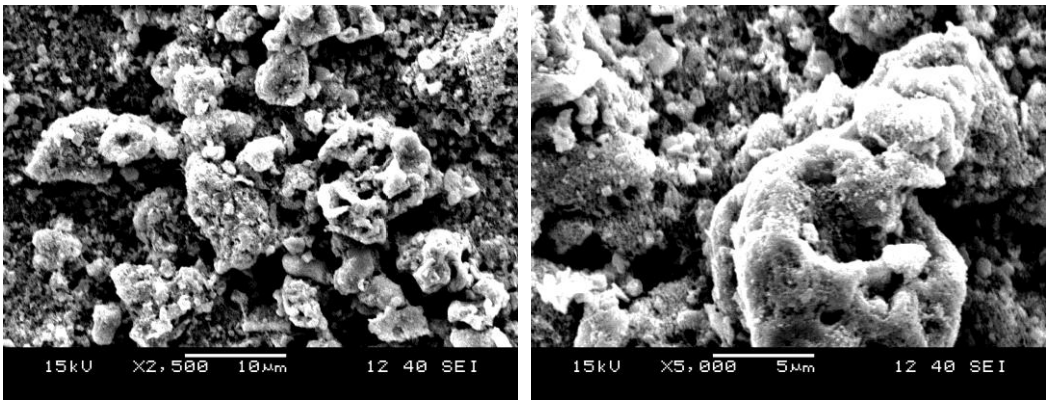

Figure 4.31 SEM images of $K_2La_{1.9}Gd_{0.1}Ti_3O_{10}$ thin film

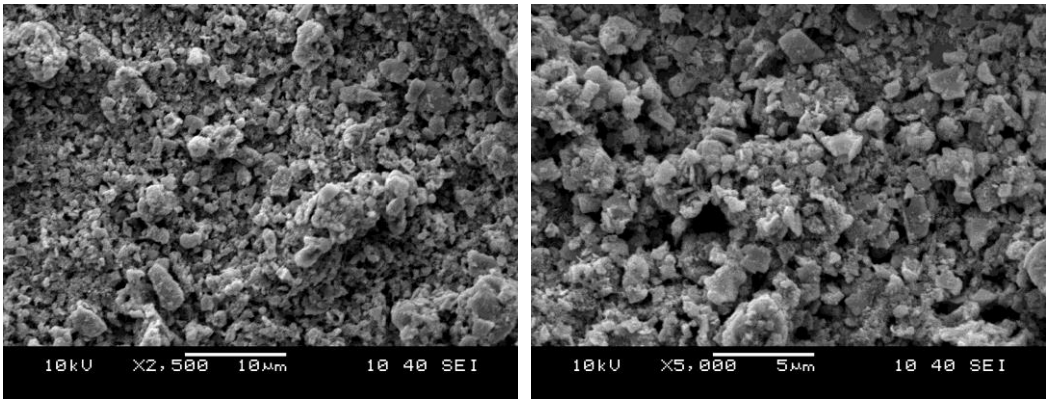

Figure 4.32 SEM images of $K_2La_{1.5}Gd_{0.5}Ti_3O_{10}$ thin film

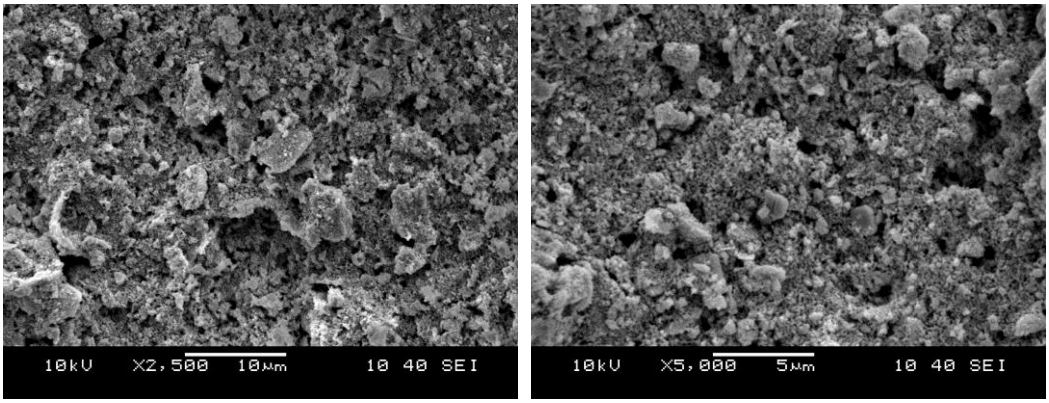

Figure 4.33 SEM images of $K_2La_{1.1}Gd_{0.9}Ti_3O_{10}$ thin film

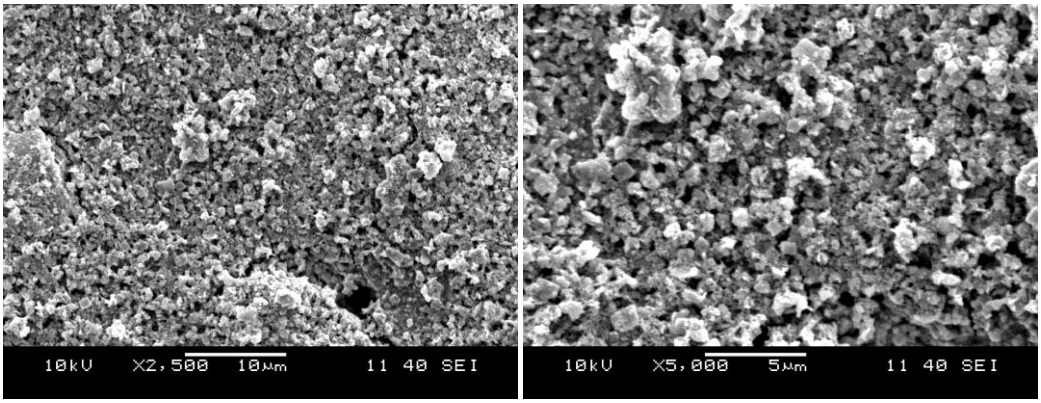

Figure 4.34 SEM images of $K_2La_{1.9}Nd_{0.1}Ti_3O_{10}$ thin film

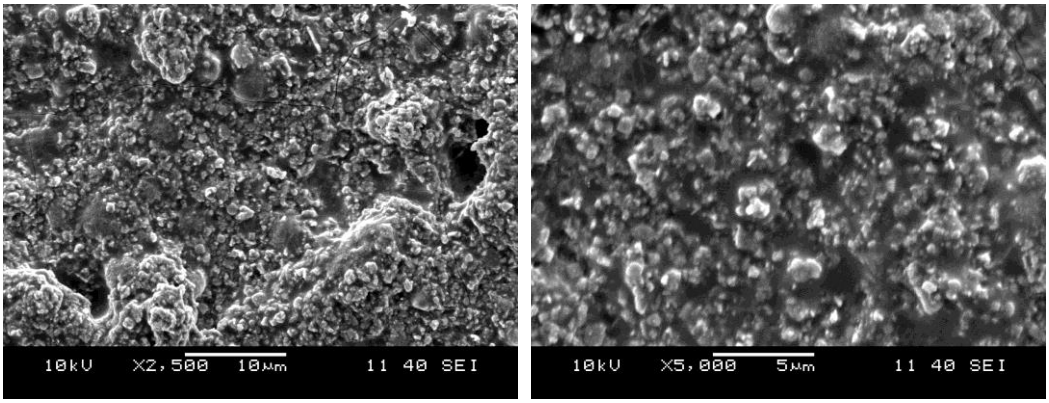

Figure 4.35 SEM images of $K_2La_{1.5}Nd_{0.5}Ti_3O_{10}$ thin film

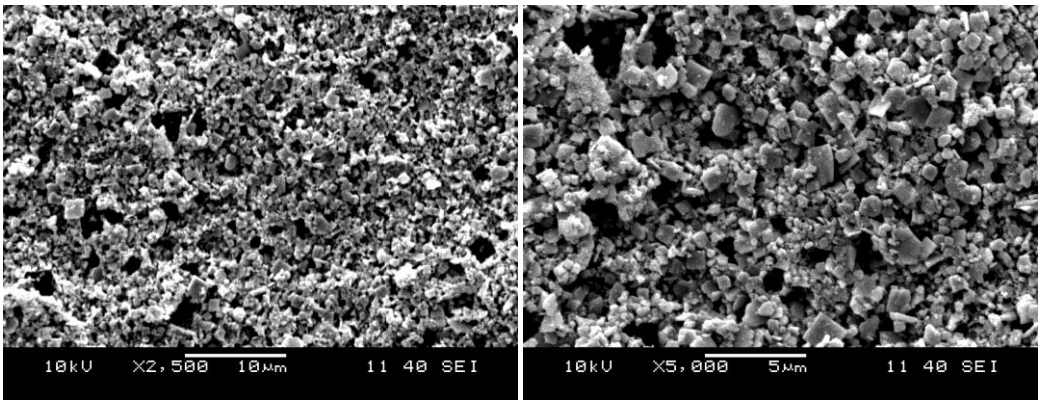

Figure 4.36 SEM images of $K_2La_{1.1}Nd_{0.9}Ti_3O_{10}$ thin film

4.2.5 Elemental Analysis

Elemental analyses of doped- KLTO were determined with the aid of XPS. The XPS analysis of $K_2Ln_2Ti_3O_{10}$ (Ln= Nd, Gd, Sm, Dy) are represented in Figures 4.37,

4.38, 4.39 and 4.40. In analysis results the presence of K, La, O and Ti elements were detected in all samples.

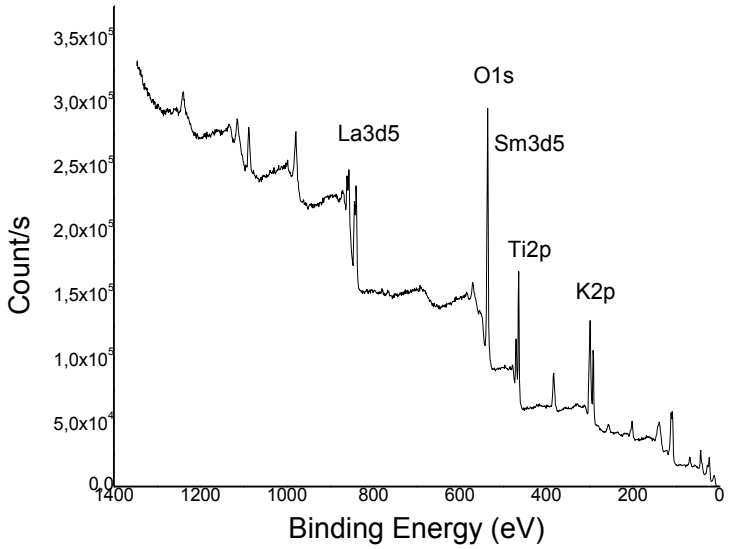

Figure 4.37 XPS analysis result of Sm-KLTO thin film

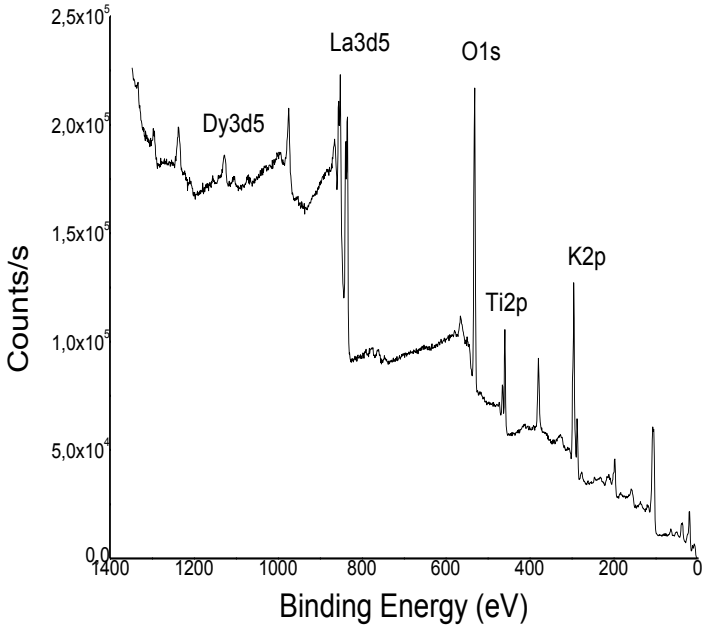

Figure 4.38 XPS analysis result of Dy-KLTO thin film

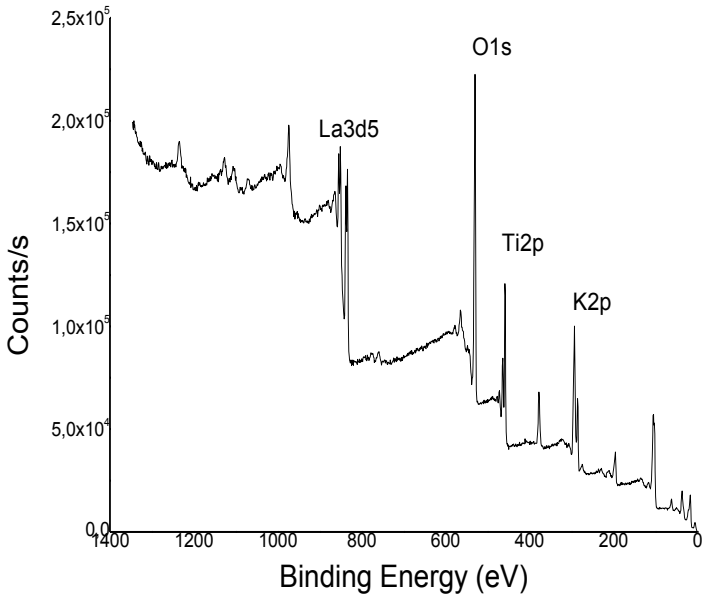

Figure 4.39 XPS analysis result of Gd-KLTO thin film

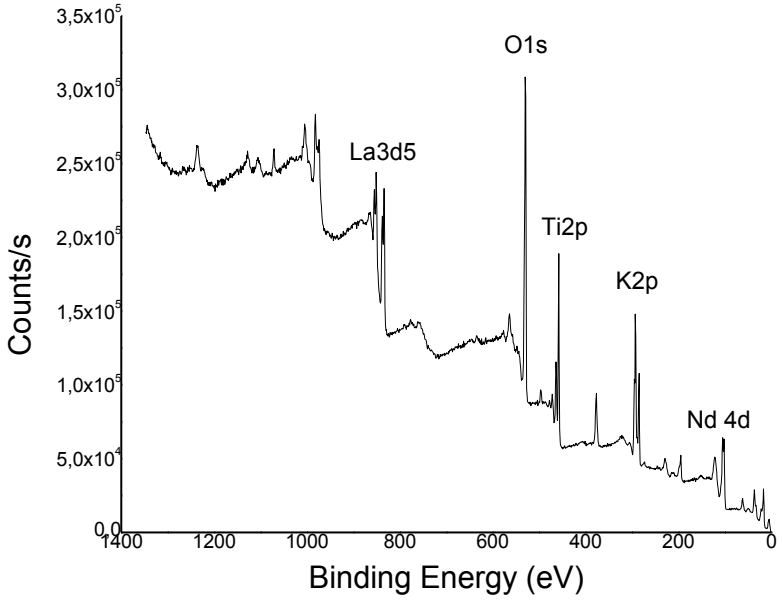

Figure 4.40 XPS analysis result of Nd-KLTO thin film

Vithal et al. (2011) observed similar spectra that exhibit characteristic Ln3d, K2p, Ti2p and O1s peaks. The La3d profiles exhibit asymmetric peaks at 839 and 856 eV which are assigned to $3d_{5/2}$ and $3d_{3/2}$ levels of La^{3+}. The $Ti2p_{3/2}$ and $2p_{1/2}$ peaks were

observed at 458.7 and 464.5eV, respectively, K 2p peak was nearly 298.11 eV were observed.

Once the XPS result was analyzed, presence of Nd, Gd, Sm, Dy elements in $K_2Ln_2Ti_3O_{10}$ proved that doping process was performed successfully. Doping elements substituted crystal lattice parameters as required without generating undesirable phases or evaporation.

4.2.6 Surface Roughness

Surface roughness is important for photocatalytic efficiency. With increasing surface area, photocatalytic efficiency increase (Hamamcı, 2008). In this study, surface roughness analyses of samples were investigated with a surface profilometer. Surface roughness, which is represented by the arithmetic mean value, R_a, and ten point mean roughness, R_z depicted in Table 4.3. When the results were analyzed, the min value of surface roughness was found 0.18 for $K_2La_{1.9}Gd_{0.1}Ti_3O_{10}$ and the max value is 1.84 μm for $K_2La_{1.9}Sm_{0.1}Ti_3O_{10}$. It is clear that, surface roughness is not depending on type and amount of dopant. It might be due to using of KLTO powder dispersed in propionic acid in coating solution.

Table 4.3 Roughness values of KLTO based samples

Sample	**R_a (μm)**	**R_z (μm)**	**Sample**	**R_a (μm)**	**R_z (μm)**
$K_2La_{1.9}Sm_{0.1}Ti_3O_{10}$	1.84	15.77	$K_2La_{1.9}Gd_{0.1}Ti_3O_{10}$	0.18	1.77
$K_2La_{1.5}Sm_{0.5}Ti_3O_{10}$	0.9	8.27	$K_2La_{1.5}Gd_{0.5}Ti_3O_{10}$	0.25	2.66
$K_2La_{1.1}Sm_{0.9}Ti_3O_{10}$	0.29	3.43	$K_2La_{1.1}Gd_{0.9}Ti_3O_{10}$	1.01	12.26
$K_2La_{1.9}Dy_{0.1}Ti_3O_{10}$	0.64	5.98	$K_2La_{1.9}Nd_{0.1}Ti_3O_{10}$	0.61	6.53
$K_2La_{1.5}Dy_{0.5}Ti_3O_{10}$	0.32	3	$K_2La_{1.5}Nd_{0.5}Ti_3O_{10}$	0.84	7.48
$K_2La_{1.1}Dy_{0.9}Ti_3O_{10}$	0.35	4	$K_2La_{1.1}Nd_{0.9}Ti_3O_{10}$	0.49	5.10

4.2.7 Mechanical Properties

As for adhesion properties of KLTO based coatings, scratch tester can be performed. In this experiment, the analysis of scratch tester gives critical force values of KLTO based specimens. The applied load (P), penetration depth (h_t), hardness (H) and modulus of elasticity (E) values belong to mechanical tests of KLTO coatings on Si(100) substrates were illustrated in Table 4.4. Nanoindentation tests were performed with different loads. Samples were measured with different penetration depths. An increase in penetration depth was generally observed with increasing of load.

The scratch test has been conventionally employed to estimate the adhesion of thin films, i.e., processes occurring at the film/substrate interface. Briefly, in a scratch test a stylus is dragged across the film surface at a constant speed, progressively increasing the normal load.

Scratch test results of $K_2Ln_2Ti_3O_{10}$ (Ln= Nd, Gd, Sm, Dy) coatings are presented in Figures 4.41 - 4.44. By using values of graphic, distance and force, the adhesion strength of the coatings was calculated by Equation 4.1 (Toparlı, 2007).

$$F = \frac{\mathrm{H}}{\sqrt{\left[\frac{\pi R^2 \mathrm{H} - \mathrm{Wc}}{\mathrm{Wc}}\right]}} \tag{4.1}$$

F: Adhesion Strength
H: Hardness (856 N.mm^{-2})
R: Radius (15 μm)
Wc: Force

As mentioned before, to overcome adhesion problems wettability is important. Higher contact angle values may lead to thicker films with high stress concentration regions. This causes mechanical failures and adhesion problems. Depending on this, film quality decreases. Sol-gel process can produce thin bond coating to provide

excellent adhesion between the metallic substrate and the top coat (Bhuiyan, Paranthaman & Salama, 2006).

Table 4.4 Mechanical values of samples (P, h_t, E, H)

Sample	P (mN	h_t (µm)	E (GPa)	H (GPa)	Sample	P (mN	h_t (m)	E (GPa)	H (GPa)
	2	1.06	7.98	0.07		2	0.92	4.54	0.12
	4	1.44	21.76	0.08		4	1.28	1.92	0.01
$K_2La_2Ti_3O_{10}$	6	2.13	15.20	0.05	$K_2La_{1.9}Gd_{0.1}Ti_3O_{10}$	6	2.12	4.35	0.05
	8	3.55	9.29	0.02		8	1.85	2.45	0.002
	10	2.54	24.35	0.06		10	5.18	3.01	0.007
	2	2.68	3.20	0.01		2	0.83	5.60	0.13
	4	2.39	3.04	0.03		4	3.49	1.84	0.01
$K_2La_{1.9}Sm_{0.1}Ti_3O_{10}$	6	3.12	4.41	0.02	$K_2La_{1.5}Gd_{0.5}Ti_3O_{10}$	6	2.43	4.39	0.04
	8	1.71	7.66	0.12		8	8.24	2.73	0.004
	10	3.90	3.04	0.02		10	7.17	2.92	0.008
	2	0.46	13.72	0.47		2	1.88	1.93	0.02
	4	4.44	1.50	0.008		4	1.34	5.39	0.10
$K_2La_{1.5}Sm_{0.5}Ti_3O_{10}$	6	3.60	3.16	0.01	$K_2La_{1.1}Gd_{0.9}Ti_3O_{10}$	6	3.25	3.32	0.024
	8	3.38	7.11	0.02		8	3.73	2.88	0.024
	10	2.38	12.6	0.07		10	4.43	3.35	0.021
	2	1.12	2.83	0.07		2	1.43	4.44	0.04
	4	2.91	1.12	0.02		4	2.34	6.64	0.03
$K_2La_{1.1}Sm_{0.9}Ti_3O_{10}$	6	8.17	0.87	0.003	$K_2La_{1.9}Nd_{0.1}Ti_3O_{10}$	6	3.14	6.29	0.025
	8	6.66	1.33	0.007		8	3.52	8.84	0.026
	10	1.16	6.93	0.43		10	1.96	19.37	0.11
	2	0.83	11.9	0.12		2	0.12	84.47	51.39
	4	2.17	8.22	0.035		4	0.27	28.69	9.94
$K_2La_{1.9}Dy_{0.1}Ti_3O_{10}$	6	2.85	8.98	0.03	$K_2La_{1.5}Nd_{0.5}Ti_3O_{10}$	6	0.41	18.48	5.22
	8	2.37	13.12	0.05		8	0.57	12.98	3.06
	10	1.92	18.91	0.11		10	0.72	10.30	2.39
	2	3.62	5.48	0.04		2	1.71	4.16	0.029
	4	3.85	5.33	0.01		4	2.76	4.61	0.021
$K_2La_{1.5}Dy_{0.5}Ti_3O_{10}$	6	2.68	2.93	0.03	$K_2La_{1.1}Nd_{0.9}Ti_3O_{10}$	6	3.42	4.70	0.021
	8	2.62	4.65	0.05		8	2.81	10.04	0.04
	10	2.14	5.51	0.09		10	4.14	7.50	0.024
	2	0.48	18.4	0.39		2	0.03	3481	434
	4	2.11	8.23	0.03		4	0.06	940	145
$K_2La_{1.1}Dy_{0.9}Ti_3O_{10}$	6	1.09	19.9	0.22	Si (100)	6	0.07	1006	162
	8	1.32	27.7	0.195		8	0.09	758	129
	10	1.47	29.3	0.195		10	0.13	447	65

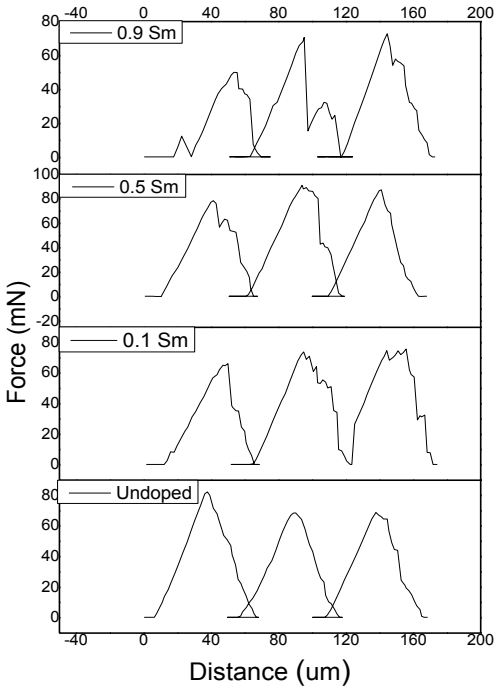

Figure 4.41 Scratch test result of Sm-KLTO thin film

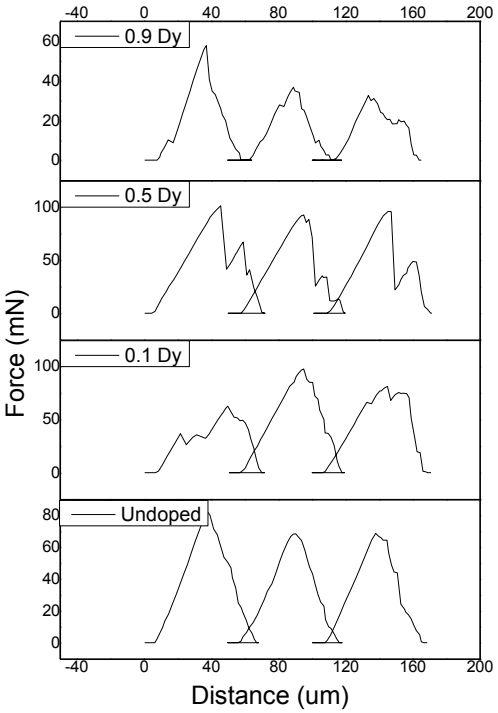

Figure 4.42 Scratch test result of Dy-KLTO thin film

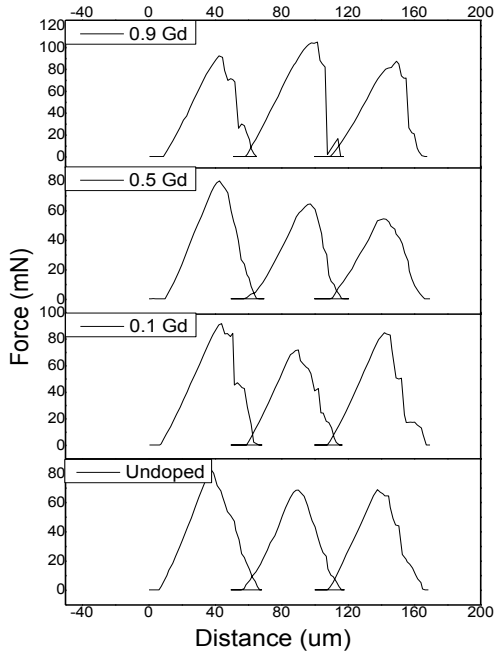

Figure 4.43 Scratch test result of Gd-KLTO thin film

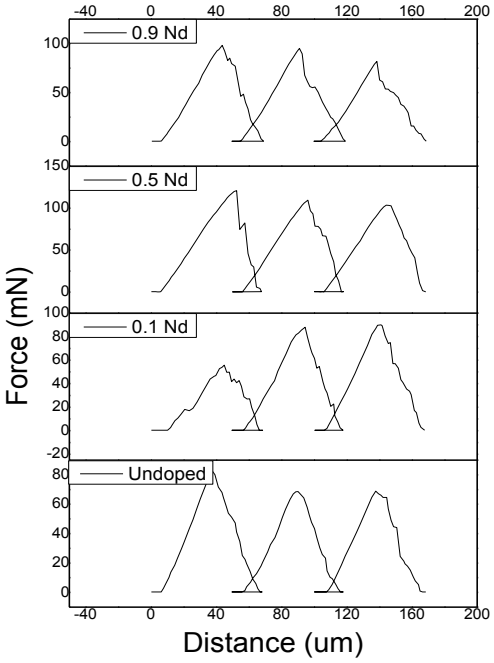

Figure 4.44 Scratch test result of Nd-KLTO thin film

Table 4.5 Adhesion strength of KLTO based thin films

Sample	Adhesion Strength (MPa)	Sample	Adhesion Strength (MPa)
$K_2La_{1.9}Sm_{0.1}Ti_3O_{10}$	251,34	$K_2La_{1.9}Gd_{0.1}Ti_3O_{10}$	278.80
$K_2La_{1.5}Sm_{0.5}Ti_3O_{10}$	312.20	$K_2La_{1.5}Gd_{0.5}Ti_3O_{10}$	284.08
$K_2La_{1.1}Sm_{0.9}Ti_3O_{10}$	215.36	$K_2La_{1.1}Gd_{0.9}Ti_3O_{10}$	339.02
$K_2La_{1.9}Dy_{0.1}Ti_3O_{10}$	281	$K_2La_{1.9}Nd_{0.1}Ti_3O_{10}$	251.34
$K_2La_{1.5}Dy_{0.5}Ti_3O_{10}$	257	$K_2La_{1.5}Nd_{0.5}Ti_3O_{10}$	329.40
$K_2La_{1.1}Dy_{0.9}Ti_3O_{10}$	166.32	$K_2La_{1.1}Nd_{0.9}Ti_3O_{10}$	302.14
$K_2La_2Ti_3O_{10}$	307.11		

Adhesion strength of $K_2La_2Ti_3O_{10}$ is 307.11. According to results, the max value is 339.02 MPa, $K_2La_{1.1}Gd_{0.9}Ti_3O_{10}$ and the min value is 166.32 MPa, $K_2La_{1.1}Dy_{0.9}Ti_3O_{10}$. Even though mechanical properties of thin films is more related to production process, adhesion strength depends on types of dopant.

It is clear that the mechanical values are not stabile. With increasing load, penetration dept is decreased. It can be resulted from inhomogeneous of coatings.

4.2.8 Optical Band Gap

Absorbance - wavelength spectrum and band gap values of $K_2Ln_2Ti_3O_{10}$ (Ln= Nd, Gd, Sm, Dy) films which were deposited on fused silica substrates were showed in Figure 4.45 and Table 4.6, respectively.

In a logical view band gap of the undoped KLTO film is higher than the substituted films. Substitution of ions in to the structure decreased band gap. It is obviously can be seen from results, when amount of dopant increased, the optical band gap decreased. It was found that the band gap of undoped KLTO was 3.73 and

band gap of $K_2La_{1.1}Dy_{0.9}Ti_3O_{10}$ was determined 3.17 as the lowest value depending on amount of dopant. Due to fact that the addition of a dopant ion, photocatalytic activity of $K_2La_2Ti_3O_{10}$ catalyst improved (Kudo, 2003).

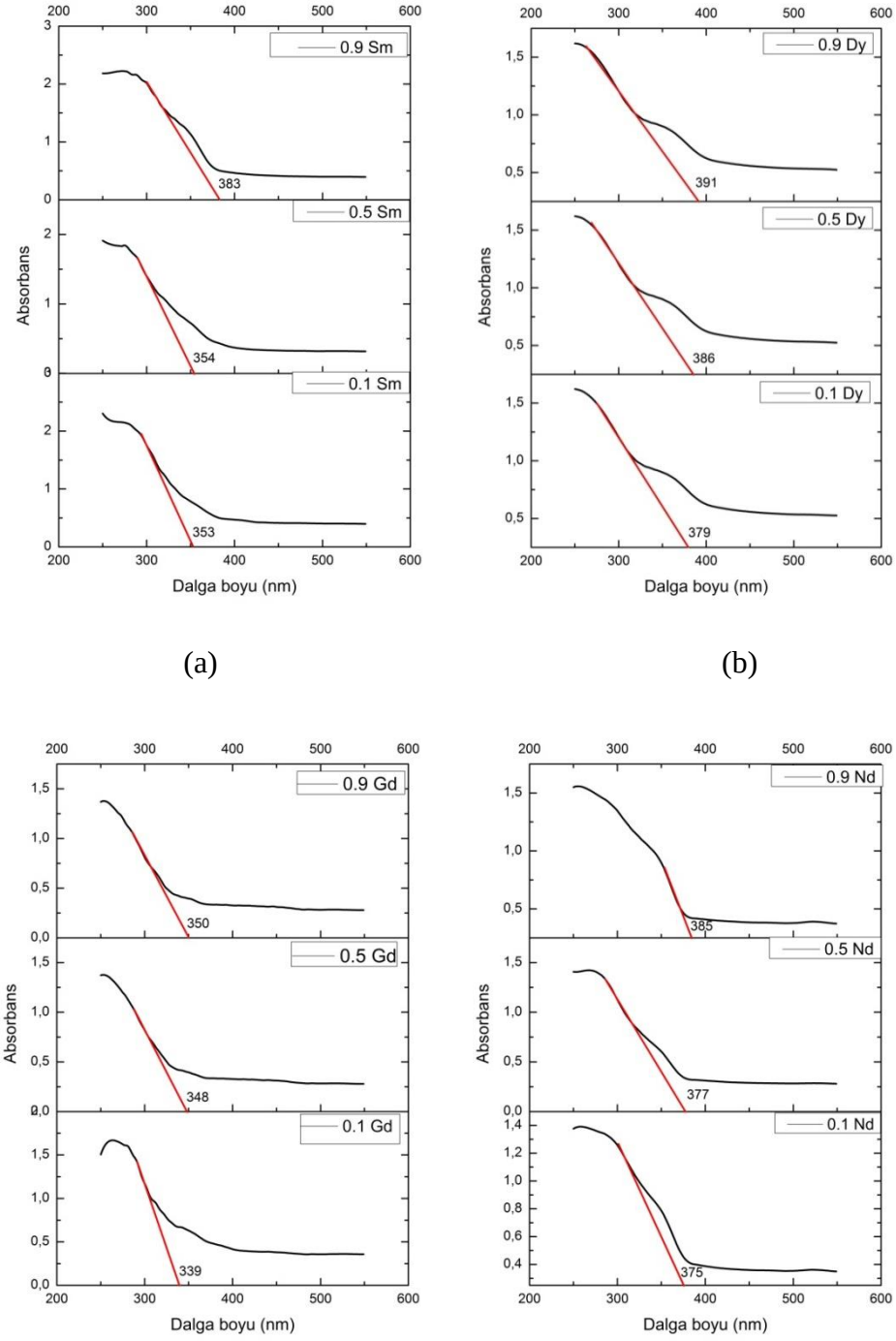

Figure 4.45 Absorbance - Wavelength spectrum of (a) Sm (b) Dy (c) Gd (d) Nd doped KLTO

Table 4.6 Band gap of thin films

Sample	Optical Band Gap (eV)	Sample	Optical Band Gap (eV)
$K_2La_{1.9}Sm_{0.1}Ti_3O_{10}$	3.51	$K_2La_{1.9}Gd_{0.1}Ti_3O_{10}$	3.65
$K_2La_{1.5}Sm_{0.5}Ti_3O_{10}$	3.50	$K_2La_{1.5}Gd_{0.5}Ti_3O_{10}$	3.56
$K_2La_{1.1}Sm_{0.9}Ti_3O_{10}$	3.23	$K_2La_{1.1}Gd_{0.9}Ti_3O_{10}$	3.54
$K_2La_{1.9}Dy_{0.1}Ti_3O_{10}$	3.27	$K_2La_{1.9}Nd_{0.1}Ti_3O_{10}$	3.30
$K_2La_{1.5}Dy_{0.5}Ti_3O_{10}$	3.21	$K_2La_{1.5}Nd_{0.5}Ti_3O_{10}$	3.28
$K_2La_{1.1}Dy_{0.9}Ti_3O_{10}$	3.17	$K_2La_{1.1}Nd_{0.9}Ti_3O_{10}$	3.22
$K_2La_2Ti_3O_{10}$	3.73		

4.2.9 Photocatalytic Result

For every catalyst, the beakers were filled till 25 ml and it was placed on the testing apparatus as shown in Figure 4.46.

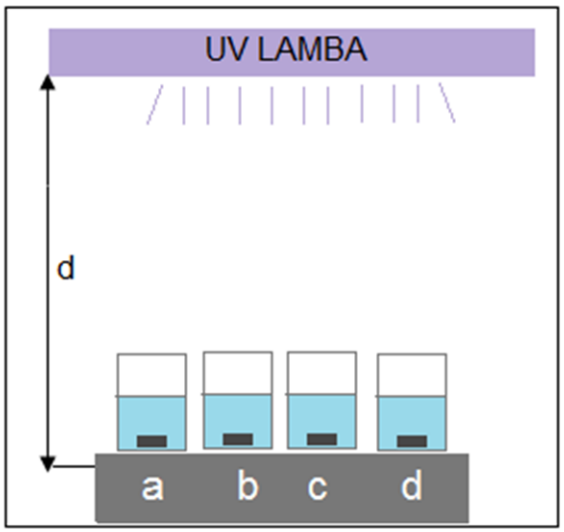

Figure 4.46 Schematic experiment apparatus (Nimetoğlu, 2011).

All photocatalytic experiments were examined by ATLAS SUNTEST CPS+. To see the difference and to make a deduction, an reference specimen (without catalyst) was carried out for every experiment. The pH was selected10 because decolorization was the fastest at pH 10, it was also reported by Hustert & Zepp (1992) and Tang & An (1995) for acidic azo dyes bearing sulfonate groups, whose degradation was the fastest at more alkaline pHs. The light intensity was selected 750 W/m^2.

The initial concentration of MB was adjusted to 10^{-5} M. The photocatalytic degradation efficiency of MB decreases with an increase in the initial concentration of MB. This can be as a result of blocking of the photocatalytically active sites on the catalyst and reducing the interaction of photons with these sites. Besides, a fraction of light may be absorbed by the MB molecules in aqueous solution rather than the catalyst particles for high MB concentration, which can also reduce the efficiency of the photocatalytic reaction to a certain extent (Wang et. al, 2013).

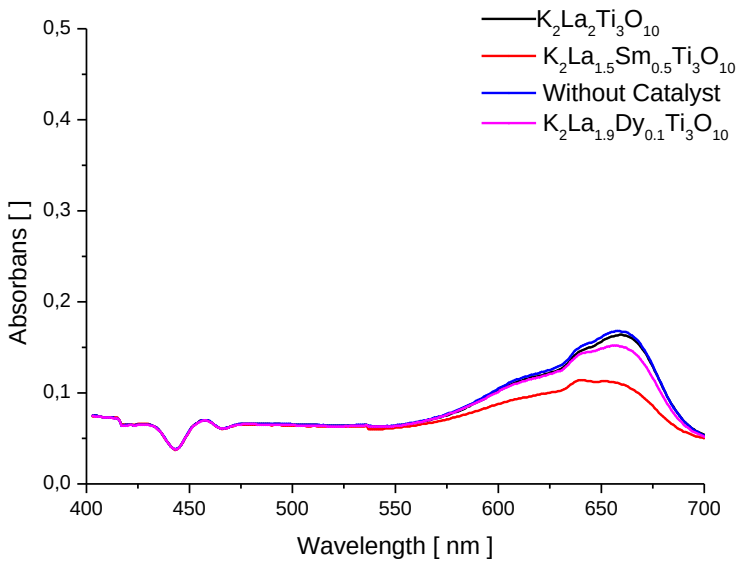

Figure 4.47 Degradation behaviours of methylene blue at pH 10, 750 W/m^2

The degradation was determined as, calculating with $[(A_0- A)/A_0]$, where A_0 and A were the absorbance of the primal and remaining MB, respectively. The

photocatalytic degradation of methlylene blue by using $K_2Ln_2Ti_3O_{10}$ (Ln= Nd, Gd, Sm, Dy) films is shown in Figure 4.47 and 4.48.

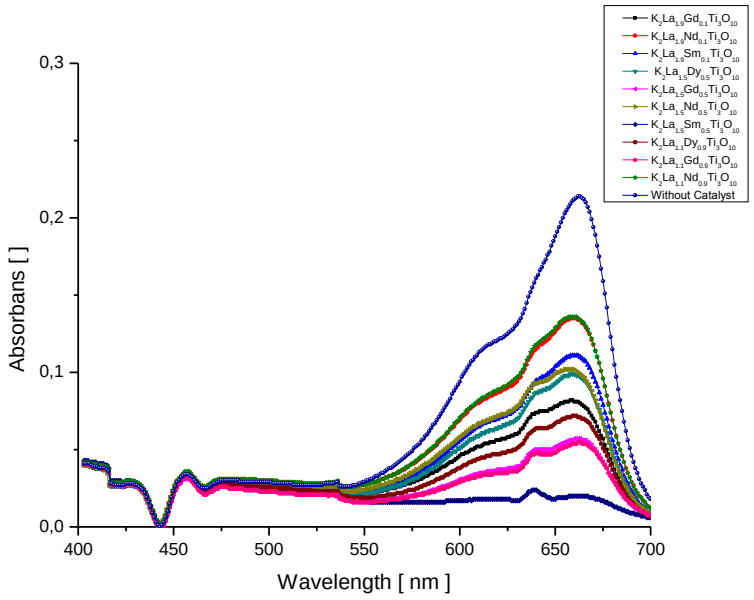

Figure 4.48 Degradation behaviours of methylene blue at pH 10, 750 W/m^2

Table 4.7 shows methylene blue degradation efficiencies at 750 W/m^2 light intensity.

Table 4.7 Degradation ratio of methylene blue at 750 W/m^2

Samples	**Degradation Ratio (%)**	**Samples**	**Degradation Ratio (%)**
$K_2La_2Ti_3O_{10}$	81	$K_2La_{1.9}Gd_{0.1}Ti_3O_{10}$	89
$K_2La_{1.9}Sm_{0.1}Ti_3O_{10}$	85	$K_2La_{1.5}Gd_{0.5}Ti_3O_{10}$	93
$K_2La_{1.5}Sm_{0.5}Ti_3O_{10}$	97	$K_2La_{1.1}Gd_{0.9}Ti_3O_{10}$	93
$K_2La_{1.1}Sm_{0.9}Ti_3O_{10}$	87	$K_2La_{1.9}Nd_{0.1}Ti_3O_{10}$	82
$K_2La_{1.9}Dy_{0.1}Ti_3O_{10}$	80	$K_2La_{1.5}Nd_{0.5}Ti_3O_{10}$	87
$K_2La_{1.5}Dy_{0.5}Ti_3O_{10}$	87	$K_2La_{1.1}Nd_{0.9}Ti_3O_{10}$	82
$K_2La_{1.1}Dy_{0.9}Ti_3O_{10}$	91	Without catalyst	71

It was found that, the maximum degration rate of methylene blue was obtained with $K_2La_{1.5}Sm_{0.5}Ti_3O_{10}$, 97 % and the minimum rate was obtained with $K_2La_2Ti_3O_{10,}$ 81 % and reference (without catalyst) rate is 71 %. As can be seen from Table 4.7, doping with Nd, Sm, Dy, Gd on $K_2La_2Ti_3O_{10}$ improved photocalytic activity and $K_2La_{1.5}Sm_{0.5}Ti_3O_{10}$ was found as the most efficient catalysis.

CHAPTER FIVE
CONCLUSION AND FUTURE PLANS

5.1 General Results

In this study, synthesis of $K_2Ln_2Ti_3O_{10}$ (Ln= Nd, Gd, Sm, Dy) films by sol-gel technique and their photocatalytical properties were investigated for coated specimens. The following conclusions are obtained from the experimental works:

1) Turbidity value of the KLTO based solution was measured as min 15.72 and as max 35.23 ntu. This values pointed that powder based precursors are almost completely dissolved in solution and the brown color of the potassium based precursor increased the turbidity.The pH value of the solution was found to be for KLTO based solutions min 3.08 and max 4.42. This pH measurement results pointed that the solution is acidic. Contact angle value of KLTO solution is lower than 90^O; therefore it is possible to express that this solution can wet the Si(100) substrates. Higher contact angle values may lead to thicker films with high stress concentration regions.The average viscosity value of KLTO solution was found to be 0.3 Pa.s. This low viscosity value is advantageous for thin film production in collaboration with low contact angle value.

2) The heat treatment regime and final sintering temperature was determined with the help of previous literature works, FTIR results and the DTA-TGA results. 1000 ^oC was determined as final phase transformation temperature.

3) XRD analysis was carried out to determine the sample phase composition. According to XRD results, KLTO thin films were synthesized successfully. In order to measure the chemical or electronic state of surface elements XPS was used. As a result of the analysis, it was seen that the results obtained are consistent with the stoichiometric ratio of the powders.

4) Depending on the SEM micrographs of the films one can express coating process and heat treatment regime are directly in a relation with microstructure.

5) The min values of surface roughness was found 0.18 and the max value is 1.84 μm. It was found that the band gap of undoped KLTO was 3.73 and band gap of $K_2La_{1.1}Dy_{0.9}Ti_3O_{10}$ was determined 3.17 as the lowest value depending on amount of dopant.

6) It was found that, the maximum degration rate of methylene blue was obtained with $K_2La_{1.5}Sm_{0.5}Ti_3O_{10}$, % 97 and the minimum rate was obtained with $K_2La_2Ti_3O_{10,}$ % 81 and reference (without catalyst) rate is % 71.

5.2 Future Plans

To conclude, the transfer of photocatalytic thin films to the industrial applications is the main aim of the studies in this field. After optimising all parameters, it is going to be possible to prepare prototip applications of these films. It is recommended that a further study should be carried out to obtain more homogeneous and well crystalized KLTO films . With this aim, new coating solutions can be prepared with different pH, viscosity and contact angle values. Except solutions, coating procedure parameters should be changed. Also, heat treatment regime should be optimized to decrease thermal shock risks. If the mentioned problems were handled, efficiency of thin films could be increased.

REFERENCES

Bakuy, Ş. (2009). *Kirli su temizleme uygulamaları için cam altlıklar üzerine Ru-TiO_2 ince film üretimi ve fotokatalitik özelliklerinin incelenmesi.* Dissertation Thesis, Dokuz Eylül University, İzmir.

Besergil, B. (2015). *FTIR Absorbsiyon Spektroskopisi*. Retrieved August 23, 2015, from http://www.bayar.edu.tr/besergil/IR_4_FTIR.pdf

Bhuiyan, M. S., Paranthaman M., & Salama, K. (2006). Solution-derived textured oxide thin films-a review. *Superconducting Science Technology*, *19*, R1-R21.

Birlik, I. (2011). *Synthesis of superconducting films and improvement of their flux pinning properties with $BaZrO_3$ nanoparticles using chemical solution deposition method.* Ph.D Thesis, Dokuz Eylül University, İzmir.

Breault, T. M. (2013). *Complex metal oxides for photocatalytic applications*. Ph.D Thesis, University of Michigan, USA.

Chen, X., Lou, Y.B., Samia, A.C.S., Burda, C., & Gole, V.L. (2005). Formation of oxynitride as the photocatalytic enhancing site in nitrigen-doped titania nanocatalysts: Comparison to a commercial nanopowder. *Advanced FunctionalMaterials, 15,* 41–49.

Crist, B.V. (2015). *X-ray photoelectron spectroscopy*. Retrieved July 20, 2015, from http://en.wikipedia.org/wiki/X-ray_photoelectron_spectroscopy

Cui, W., Liu, L., Ma, S., Liang, Y., & Zhang, Z. (2012). CdS-sensitized $K_2La_2Ti_3O_{10}$ composite: A new photocatalyst for hydrogen evolution under visible light irradiation. *Catalysis Today, 207,* 44–49.

Domen, K., Furumi, Y., Shinohara, K., Tanaka, A., Hara, M., & Kondo, J.N.(1997). Photocatalytic decomposition of water on spontaneously hydrated layered perovskites. *Chemistry of Materials*, *9*, 1063-1064.

Ebeoglugil, M. F. (2011). *Processing, characterization and development of rare earth doped lead magnesium niobate ferroelectric ceramic capacitors by sol-gel technique*. Ph.D Thesis, Dokuz Eylül University, İzmir.

Erol, M. (2009). *Synthesis of garnet based films by sol-gel technique and investigation of their magneto-optic properties*. M.Sc.Thesis, Dokuz Eylül University, İzmir.

Fujihara, S., Sasaki, C.,& Kimura, T. (2001).Crystallization behavior and origine of c-axis orientation in sol-gel derived ZnO:Li thin films on glass substrates. *Applied Surface Science*, *180*, 341-350.

Hamamcı, A.K. (2008). *Antibakteriyel uygulamalar için cam altlıklar üzerine V katkılı TiO_2 ince film üretimi ve fotokatalitik özelliklerinin incelenmesi*, Dissertation Thesis, Dokuz Eylül University, İzmir.

Haque, M. M., Bahnemann, D., & Muneer, M. (2012). *Photocatalytic degradation of organic pollutants: Mechanisms and kinetics, organic pollutants ten years after the Stockholm convention - Environmental and Analytical Update*, Dr. Tomasz Puzyn (Ed.), China: InTech.

Hustert, K., & Zepp, R.G. (1992). Photocatalytic degradation of selected azo dyes. *Chemosphere*, *24*, 335–342.

Kudo, A., & Miseki, Y. (2009). Heterogeneous photocatalyst materials for water splitting. *Chemical Society Reviews*, *38*, 253–278.

Kudo, A. (2003). Photocatalyst materials for water splitting . *Catalysis Surveys from Asia, 7,* 31-38.

Lee, J., Kim, H., Hwang, D., Bae, S., & Jung, J. (2003). Photocatalytic water splitting over $La_2Ti_2O_7$ synthesized by the polymerizable complex method. *Catalysis Letters, 91,* 193–198.

Li, Y., Huang, Y., Wei, Y., Cheng, S., Fan, L., Wun, J. et al. (2010). Photocatalytic property of nitrogen-doped layered perovskite $K_2La_2Ti_3O_{10}$. *Solar Energy Materials & Solar Cells, 94,* 761–766.

Marschall, R., & Wang L. (2013). Non-metal doping of transition metal oxides for visible- light photocatalysis. *Catalysis Today, 225,* 111-135.

Miller, E.L. (2012). Multijunction approaches to photoelectrochemical water splitting. R. van de Krol and M. Gratzel (Eds.), *Photoelectrochemical Hydrogen Production* (205-277). New York : Springer.

Neiner, D. (2005). *New Ruddlesden-Popper perovskites obtained by topochemical methods*. Ph.D Thesis, University of New Orleans, USA

Nimetoğlu, Z. (2011). *Yeni nesil fotokatalitik filmlerin üretilmesi ve atıksulardaki organik kirleticilerin temizlenmesinde kullanılması.* Disertation Thesis, Dokuz Eylül University, İzmir.

Pierre, A. C. (1998). *Introduction to sol-gel processing*. USA: Kluwer Academic Publishers.

Tang, W.Z., & An, H. (1995). Photocatalytic degradation kinetics and mechanism of acid blue 40 by TiO_2/UV in aqueous solution. *Chemosphere, 31,* 4171–4183.

Toparlı, M., Sen, F., Culha, O., & Celik, E. (2007). Thermal stress analysis of HVOF sprayed WC–Co/NiAl multilayer coatings on stainless steel substrate using finite element methods. *Journal of Materials Processing Technology, 190*, 26-32.

Uma, S., Kumar, V., & Govind. (2011). Investigation of cation (Sn^{2+}) and anion (N^{3-}) substitution in favor of visible light photocatalytic activity in the layered perovskite $K_2La_2Ti_3O_{10}$. *Journal of Hazardous Materials, 189*, 502–508.

Vithal, M., Kumar, B., Velchuri, R., Devi, V. R., Sreedhar, B., Prasad G., et al. (2011). Preparation, characterization, magnetic susceptibility (Eu,Gd and Sm) and XPS studies of Ln_2ZrTiO_7 (Ln = La, Eu, Dy and Gd). *Journal of Solid State Chemistry, 184*, 264–272.

Wu, J., Huang, Y., Wei, Y., Lin, J., & Huang, M. (2008).Hydrothermal synthesis of $K_2La_2Ti_3O_{10}$ and photocatalytic splitting of water. *Journal of Alloys and Compounds, 456*, 364–367.

Wang, B., Li, C., Hirabayashi D., & Suzuki, K. (2010). Hydrogen evolution by photocatalytic decomposition of water under ultraviolet–visible irradiation over $K_2La_2Ti_{3-x}M_xO_{10+\delta}$ perovskite. *International Journal of Hydrogen Energy, 35*, 3306-3312.

Wang, H.-L., Zhao D., & Jiang, W. (2013). VIS-light-induced photocatalytic degradation of methylene blue (MB) dye using PoPD/TiO_2 composite photocatalysts. *Desalination and Water Treatment, 51*, 2826-2835.

Wang, L., & Zong, X. (2014). Ion-exchangeable semiconductor materials for visible light- induced photocatalysis. *Journal of Photochemistry and PhotobiologyC:Photochemistry Reviews, 18*, 32–49.

Yao, J., & Wang, C. (2010). Decolorization of methylene blue with TiO_2 sol via UV irradiation photocatalytic degradation. *International Journal of Photoenergy, 2010*, 6-12.

Yang, Y.H., Qiu, G.Z., Chen, Q.Y, Feng, Q.M., & Yin, Z.L. (2007). Influence of calcination atmosphere on photocatalytic reactivity of $K_2La_2Ti_3O_{10}$ for watersplitting. *Transactions of Nonferrous Metals Society of China*, *17*, 836-840.

Yang,Y., Chen,Q.,Yin, Z., & Li, J. (2009). Study on the photocatalytic activity of $K_2La_2Ti_3O_{10}$ doped with zinc (Zn). *Applied Surface Science*, *255*, 8419-8424.